An ex vivo system to study cellular dynamics underlying mouse peri-implantation development

AUTHOR(S):

Ichikawa, Takafumi; Zhang, Hui Ting; Panavaite, Laura; Erzberger, Anna; Fabrèges, Dimitri; Snajder, Rene; Wolny, Adrian; ... Hufnagel, Lars; Kreshuk, Anna; Hiiragi, Takashi

CITATION:

Ichikawa, Takafumi ...[et al]. An ex vivo system to study cellular dynamics underlying mouse peri-implantation development. Developmental Cell 2022, 57(3): 373-386: e9.

ISSUE DATE:

2022-02

URL:

http://hdl.handle.net/2433/267903

Resource

Developmental Cell

An *ex vivo* system to study cellular dynamics underlying mouse peri-implantation development

Graphical abstract

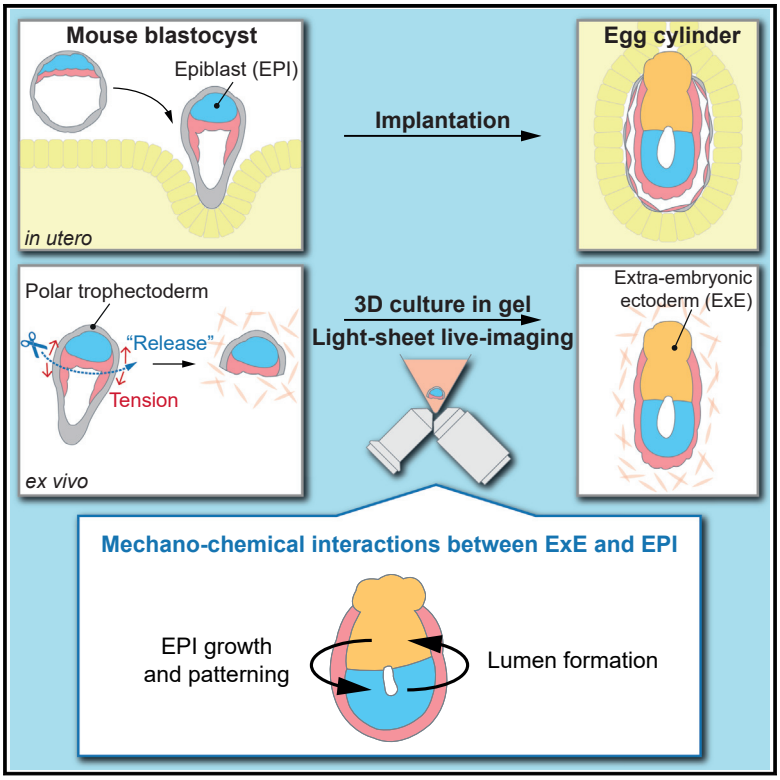

Authors

Takafumi Ichikawa, Hui Ting Zhang, Laura Panavaite, ..., Lars Hufnagel, Anna Kreshuk, Takashi Hiiragi

Correspondence

erzberger@embl.de (A.E.), t.hiiragi@hubrecht.eu (T.H.)

In brief

Ichikawa et al. establish a 3D *ex vivo* culture that recapitulates mouse peri-implantation embryo development. Light-sheet microscopy reveals dynamic cellular coordination underlying epiblast order emergence. Tension release in the polar trophectoderm allows its development into the extra-embryonic ectoderm, which later guides epiblast growth and patterning through mechano-chemical interactions.

Highlights

- A 3D culture in gel recapitulates mouse peri-implantation embryo development
- Tension release in the trophectoderm enables extra-embryonic ectoderm formation
- Light-sheet microscopy reveals dynamic coordination for epiblast order emergence
- Key mechano-chemical interactions between embryonic and extra-embryonic tissues

Ichikawa et al., 2022, Developmental Cell *57*, 373–386
February 7, 2022
https://doi.org/10.1016/j.devcel.2021.12.023

CellPress

Developmental Cell
CellPress OPEN ACCESS

Resource

An *ex vivo* system to study cellular dynamics underlying mouse peri-implantation development

Takafumi Ichikawa,[1,4,11] Hui Ting Zhang,[1,3,11] Laura Panavaite,[1,3,5,11] Anna Erzberger,[1,*] Dimitri Fabrèges,[1] Rene Snajder,[1,6] Adrian Wolny,[1] Ekaterina Korotkevich,[1,7] Nobuko Tsuchida-Straeten,[1,8] Lars Hufnagel,[1,9] Anna Kreshuk,[1] and Takashi Hiiragi[1,2,10,12,*]

[1]European Molecular Biology Laboratory (EMBL), 69117 Heidelberg, Germany
[2]Institute for the Advanced Study of Human Biology (WPI-ASHBi), Kyoto University, 606-8501 Kyoto, Japan
[3]Collaboration for PhD degree between EMBL and Heidelberg University, Faculty of Biosciences, Heidelberg, Germany
[4]Present address: Institute for the Advanced Study of Human Biology (WPI-ASHBi), Kyoto University, Kyoto, Japan
[5]Present address: BioNTech, Mainz, Germany
[6]Present address: Deutsches Krebsforschungszentrum, Heidelberg, Germany
[7]Present address: University of California, San Francisco, San Francisco, CA, USA
[8]Present address: Institut für Humangenetik, Universitätsklinikum Heidelberg, Heidelberg, Germany
[9]Present address: Luxendo, Bruker, Germany
[10]Present address: Hubrecht Institute, KNAW (Royal Netherlands Academy of Arts and Sciences), Utrecht, the Netherlands
[11]These authors contributed equally
[12]Lead contact
*Correspondence: erzberger@embl.de (A.E.), t.hiiragi@hubrecht.eu (T.H.)
https://doi.org/10.1016/j.devcel.2021.12.023

SUMMARY

Upon implantation, mammalian embryos undergo major morphogenesis and key developmental processes such as body axis specification and gastrulation. However, limited accessibility obscures the study of these crucial processes. Here, we develop an *ex vivo* Matrigel-collagen-based culture to recapitulate mouse development from E4.5 to E6.0. Our system not only recapitulates embryonic growth, axis initiation, and overall 3D architecture in 49% of the cases, but its compatibility with light-sheet microscopy also enables the study of cellular dynamics through automatic cell segmentation. We find that, upon implantation, release of the increasing tension in the polar trophectoderm is necessary for its constriction and invagination. The resulting extra-embryonic ectoderm plays a key role in growth, morphogenesis, and patterning of the neighboring epiblast, which subsequently gives rise to all embryonic tissues. This 3D *ex vivo* system thus offers unprecedented access to peri-implantation development for *in toto* monitoring, measurement, and spatiotemporally controlled perturbation, revealing a mechano-chemical interplay between extra-embryonic and embryonic tissues.

INTRODUCTION

Implantation is a unique event in mammalian development whereby an exchange interface is established between the embryo and the maternal tissues (Hemberger et al., 2020; Wang and Dey, 2006). In the first few days following fertilization, the pre-implantation embryo develops into a fluid-filled blastocyst wherein the pluripotent epiblast (EPI) is sandwiched between the outer trophectoderm (TE) and the primitive endoderm (PrE). Upon implantation, the extra-embryonic portion of the embryo, consisting of TE and PrE-derived cells, engages the maternal tissue in a complex interplay that eventually forms the placenta. In the embryo proper, implantation coincides with major changes in tissue architecture as it undergoes gastrulation and body axes specification (Arnold and Robertson, 2009; Rossant and Tam, 2009; Takaoka and Hamada, 2012). Though genetic studies characterized key genes and signaling pathways required for these processes, their underlying cellular mechanisms remain obscured by inaccessibility to the implantation process.

Ex vivo culture provides an experimental setting to monitor, measure, and manipulate embryonic development to glean mechanistic insight. *Ex vivo* culture of peri-implantation mouse embryos so far relied on embryonic growth on 2D surfaces (Bedzhov and Zernicka-Goetz, 2014; Hsu, 1971, 1972; Morris et al., 2012; Pienkowski et al., 1974; Tachi, 1992). This culture typically induces adhesion and spread of trophoblast cells over the surface, disrupting embryonic morphogenesis. Therefore, recapitulation of *in vivo* development is limited with current methods, both in terms of efficiency and physiological relevance.

In toto live-imaging has been carried out for later post-implantation mouse development using light-sheet microscopes (Ichikawa et al., 2013; McDole et al., 2018; Udan et al., 2014; Yue et al., 2020). However, these experimental settings limit the sample number and do not allow quantitative analyses of cellular and tissue morphogenesis or spatiotemporally controlled perturbations. Furthermore, though many studies have introduced new experimental systems focused on the development of embryonic tissues (van den Brink et al., 2014; Deglincerti et al., 2016;

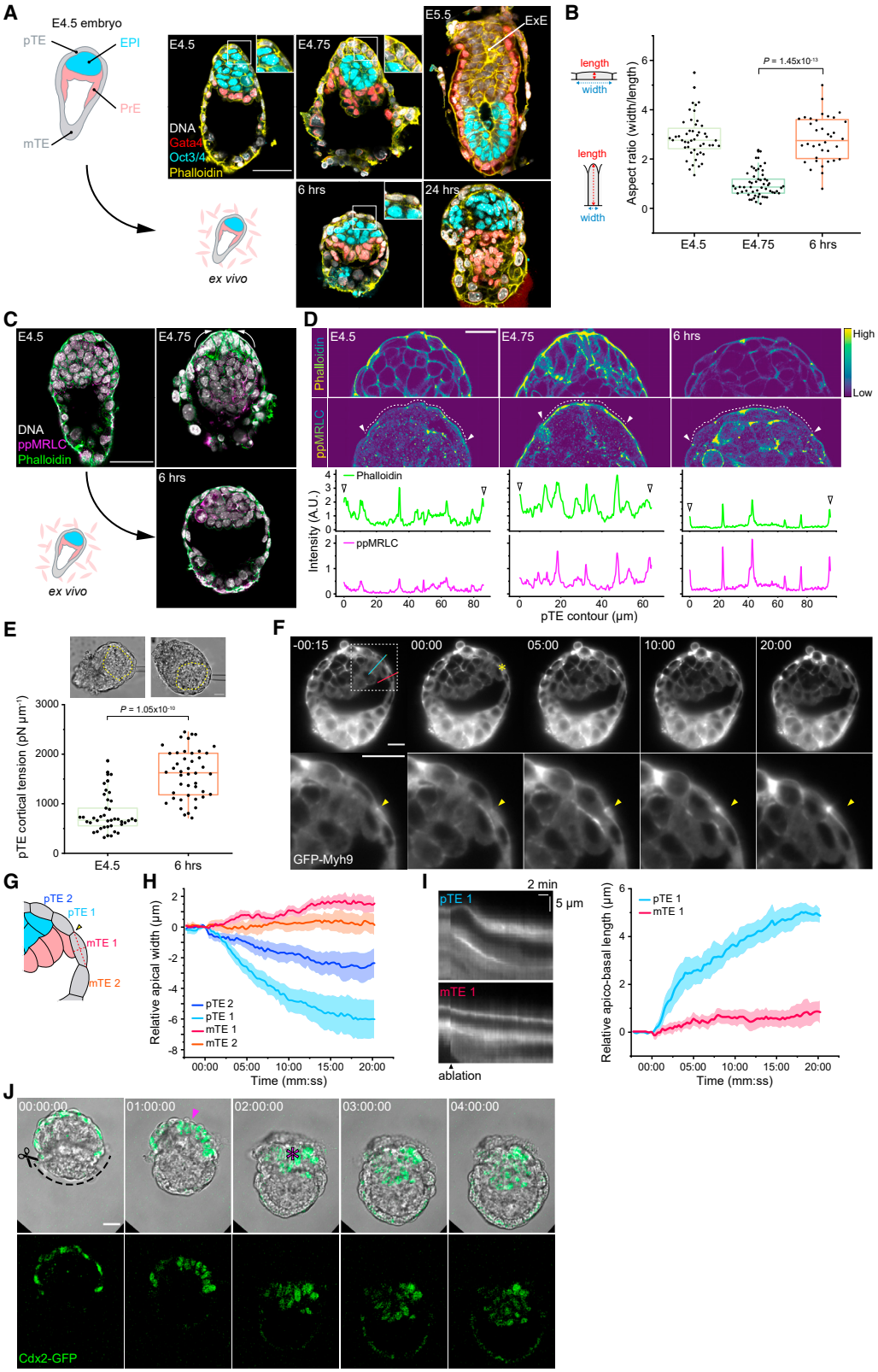

Figure 1. Trophectoderm tension release enables invagination and formation of the extra-embryonic ectoderm

(A) Representative images of mouse embryos developed *in utero* (top) in comparison with those cultured in 3D in Matrigel and collagen mix from E4.5 (bottom), immunostained for Oct3/4^{+} EPI, Gata4^{+} VE, actin, and DNA. n = 20 (E4.5), 23 (E4.75), 25 (E5.5), 12 (6 h), and 18 (24 h), respectively.

(legend continued on next page)

Shahbazi et al., 2016; Warmflash et al., 2014; Zheng et al., 2019), the contributions of extra-embryonic or uterine tissues in embryonic development have been relatively overlooked, largely due to technical challenges (Brennan et al., 2001; Christodoulou et al., 2019; Guzman-Ayala et al., 2004; Hiramatsu et al., 2013; Thomas and Beddington, 1996). It remains to be examined how interactions between embryonic and extra-embryonic tissues influence mammalian peri-implantation development.

It is evident that tissue interactions are vital throughout development. Morphogenesis induces spatiotemporally coordinated tissue-tissue interactions that feed back on cellular behaviors such as differentiation and cellular rearrangement, which in turn guide morphogenesis (Bailles et al., 2019; Eiraku et al., 2011; Harland and Gerhart, 1997; Münster et al., 2019; Saunders and Gasseling, 1968; Shyer et al., 2015). To study such an interaction between embryonic and extra-embryonic tissues, it is essential to have an experimental system that faithfully recapitulates peri-implantation development *ex vivo*. Furthermore, the system must be compatible with live monitoring, measurement, and perturbation tools to provide mechanistic insights into relevant processes.

In this study, we developed a 3D culture method for mouse peri-implantation embryos that can couple to *in toto* light-sheet live-imaging. Quantitative analyses of tissue dynamics at single-cell resolution and biophysical measurements and perturbations revealed a key role for mechano-chemical interactions between embryonic and extra-embryonic tissues during early mammalian development.

RESULTS

Tension release in the trophectoderm enables invagination and formation of the extra-embryonic ectoderm

With the goal of recapitulating *in utero* development *ex vivo*, we attempted to culture peri-implantation mouse embryos while maintaining their 3D-morphology. Blastocysts developed *in utero* up to embryonic day 4.5 (E4.5) were recovered and embedded into a mixture of Matrigel and collagen. Their development was compared with embryos *in utero* at equivalent stages, undergoing implantation and egg cylinder formation. After 24 h of culture, however, this *ex vivo* condition failed to support proper embryonic development, resulting in disorganized morphology and deterioration of the EPI (Figure 1A). To improve this culture method, we compared embryos at early stages of culture with corresponding stages of *in utero* developed embryos. We found that the polar trophectoderm (pTE) cells do not invaginate and thus fail to form the extra-embryonic ectoderm (ExE) after 6 h in culture, unlike E4.75 embryos developed *in utero* (Figures 1A and S1; Christodoulou et al., 2019; Copp, 1979). Instead, pTE cells in cultured embryos appeared highly stretched, in contrast to the columnar appearance in embryos developed *in utero* (Figure 1B). This suggested high tension acting on pTE cells in culture. Accordingly, actin and bi-phosphorylated myosin regulatory light chain (ppMRLC) were enriched at the apical surface of the pTE cells before and during invagination in *in utero* developed embryos, whereas they were localized at cell-cell junctions in those developed *ex vivo* (Figures 1C and 1D). Furthermore, direct measurement by micropipette aspiration (Maître et al., 2015) indicated that cortical tension of pTE cells increases during this period (Figure 1E). Collectively, these findings suggest that pTE cells invaginate from the surface layer by the apical constriction, similar to *Drosophila* gastrulation (Martin et al., 2009), and that excess tension acting on pTE cells, as induced by this culture method, prevents pTE invagination and subsequent ExE formation.

This hypothesis predicts that tension release may allow pTE cells to undergo apical constriction and invagination. We tested this by using two micromanipulation methods that release TE tension at the boundary between polar and mural TEs and examined their impact at different spatiotemporal scales. First, spatiotemporally controlled infra-red laser pulses (de Medeiros et al., 2020), targeted at the TE apical cortex of the embryos cultured for 6 h, indeed induced apical constriction of pTE cells over the following 20 min (Figure 1F; Video S1). The pTE cells shortened apically and elongated along their apico-basal axis (Figures 1G–1I). Next, to examine the impact of tension release at a longer timescale, we microsurgically excised the mural trophectoderm (mTE) from E4.5 embryos at the mTE-pTE boundary. This rapidly

(B) Aspect ratio (width to length) of pTE cells in embryos developed *in utero* or in 3D gel culture shown in (A). n = 16, 18, and 12, respectively. Three pTE cells per embryo were measured.
(C) Representative images of mouse embryos developed *in utero* (top) in comparison with those cultured in 3D gel from E4.5 (bottom) immunostained for actin, bi-phosphorylated myosin regulatory light chain (ppMRLC), and DNA. Arrows indicate the apical constriction of pTE cells. n = 24 (E4.5), 34 (E4.75), and 16 (6 h), respectively.
(D) Subcellular localization of actin and ppMRLC along the apical surface of pTE cells in embryos shown in (C). Line intensity profiles obtained by tracing along the apical membrane of pTE cells (white broken lines). Peaks indicated by arrowheads in the intensity profiles (bottom) correspond to the cell-cell junctions indicated in the microscope images (top).
(E) Cortical tension of pTE cells in E4.5 embryos and embryos after 6 h of culture, measured by micropipette aspiration. n = 41 cells from 16 embryos (E4.5) and 44 cells from 18 embryos (6 h). Yellow broken lines mark the EPI.
(F) Time-lapse images of a representative GFP-Myh9 embryo after 6 h of 3D gel culture, ablated with infra-red laser pulses. Ablated point is marked with an asterisk (t = 00:00, top) and arrowheads in enlarged views (bottom). Time, minutes:seconds.
(G) Schematic for cell shape analysis of TE cells in (F).
(H) Change in the apical width of pTE cells, upon laser ablation. Data presented as mean ± SEM. n = 6.
(I) Kymographs of GFP-Myh9 signal along with blue and red lines in (F), and measurement of the apico-basal length of pTE cells upon laser ablation. Data presented as mean ± SEM. n = 6.
(J) Time-lapse images of a representative Cdx2-GFP embryo at E4.5 immediately after microsurgical removal of mTE cells, without adhesion and spreading of remaining trophectoderm. An arrowhead indicates the apically constricting pTE cells, an asterisk the invaginated ExE cells. Time, hours:minutes:seconds. n = 4.
p values calculated using Kruskal-Wallis ANOVA, followed by multiple Mann-Whitney U test (B) and Mann-Whitney U test (E). Scale bars: 50 μm in (A and C) and 20 μm in (D, E, F, and J). See also Figure S1 and Videos S1 and S2.

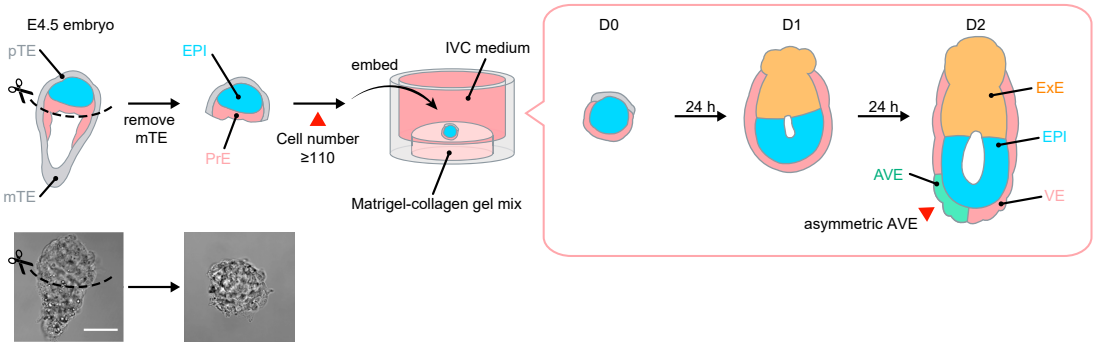

Figure 2. A new 3D *ex vivo* culture of the mouse peri-implantation embryo

Schematic of the 3D-geec workflow (top) and representative DIC images of the embryo (bottom). Mouse embryos from natural mating are recovered at E4.5. After microsurgically removing mTE, the qualified embryos, with cell number 110 or higher (see Figure S2), are embedded in a Matrigel-collagen mix and submerged in IVC medium. Embryo development is evaluated after 48 h of culture by the formation of egg cylinder (see Figure 3) and the asymmetric distribution of AVE (see Figure 4). Scale bars, 50 μm. See also Figure S2.

induced pTE cell constriction, followed by invagination after 2 h (Figure 1J; Video S2). These results support the hypothesis that pTE cells invaginate by apical constriction during implantation, which requires release of tension acting on TE cells.

We therefore decided to excise the mTE for subsequent 3D culture of peri-implantation mouse embryos. Notably, this finding that mTE removal improves *ex vivo* culture is in agreement with an earlier observation (Bedzhov et al., 2014), despite the difference between 3D and 2D culture methods. Taken together, these findings show that during mouse peri-implantation development, TE tension increases before its release enables the apical constriction of pTE cells for invagination, growth, and formation of the ExE tissue.

3D-geec recapitulates mouse peri-implantation development

We further investigated conditions optimal for robust recapitulation of peri-implantation development *ex vivo* in a 3D gel environment. We first tested blastocysts recovered at E3.5 and developed *ex vivo* for 24 h before removing the mTE (Figure S2A). However, few of these embryos developed into egg cylinders (12%, n = 4 of 33 embryos), due to their inability to recapitulate *in utero* blastocyst maturation (Figures S2B–S2H). We therefore used blastocysts recovered at E4.5 and removed their mTE for subsequent 3D culture (Figure S2I). To establish the robust culture methods, we introduced quantitative measures to define the initial embryonic parameters for successful *ex vivo* development and to evaluate the outcome after 48 h of culture (Figure 2). We found that embryos recovered at E4.5 after natural mating exhibit a high degree of variability in their progression of development, with the combined number of cells in the inner cell mass and pTE ranging from 55 to 232 (Figures S2J and S2K). The success rate of *ex vivo* culture increases with cell number at E4.5. Therefore, a high sample number and efficient *ex vivo* development can be achieved in combination when E4.5 embryos are selected for cell numbers greater than or equal to 110 (Figure S2K). Although this introduces an additional step before culture, in which the embryos are labeled with Hoechst and briefly imaged by confocal microscopy to count cell numbers, this does not compromise development (Figure S2L). Together, cell number is a reliable predictor of successful *ex vivo* development and ensures consistent and robust experimental outcomes.

With these embryos, we quantitatively evaluated the performance of our 3D *ex vivo* culture, named 3D-gel embedded embryo culture (3D-geec), in comparison with embryos developed *in utero*. Over 48 h, development in 3D-geec closely follows *in utero* developmental changes that occur from E4.5 to E6.0, as judged from embryo morphology and anterior-posterior axis specification (Figures 3A and S3A). Again, we found that *in utero* development progresses with considerable variability in embryo size and cell number (Figures 3B and 3C). The dimensions of 3D-geec embryos are largely comparable, whereas they exhibit a slightly higher diameter-to-length ratio when compared with their *in utero* counterparts (Figures 3D, S3B, and S3C). Cell numbers in the EPI and visceral endoderm (VE) show a proportional increase in 3D-geec, with 1.5 days (from E4.5 to E6.0) of *in utero* development achieved by 48 h in culture. Overall, embryonic development in 3D-geec exhibits a 25% temporal delay based on cell number (Figures 3C, 3E, and 3F), and these data offer a faithful and quantitative method to stage mouse peri- and post-implantation embryos upon recovery by cell number (Figures S3D and S3E).

We also introduced additional measures to evaluate the outcome of 3D-geec, based on cell differentiation and embryonic patterning. For this purpose, we analyzed the distribution of anterior visceral endoderm (AVE) cells in the VE after 48 h in 3D-geec. At E6.0, mouse embryos establish the anterior-posterior axis through the migration of distal VE cells to the anterior, forming the AVE (Brennan et al., 2001; Thomas et al., 1998). To quantitatively assess the anterior-posterior axis specification, we defined an AVE asymmetry index based on the 3D distribution of Lefty1- or Cerl1-expressing AVE cells relative to Gata4-expressing VE cells at the distal tip of the egg cylinder (Figures 4A and 4B). Using *in utero* developed embryos as a reference, we found that 3D-geec embryos with an AVE asymmetry index greater than 0.15 can be considered as having successfully established an asymmetric AVE distribution and thus the anterior-posterior embryonic axis (Figure 4C). Based on this criterion, 67% (n = 12 of 18) of the 3D-geec-derived egg cylinders displayed AVE asymmetry. On the other hand, 74% (n = 17 of 23)

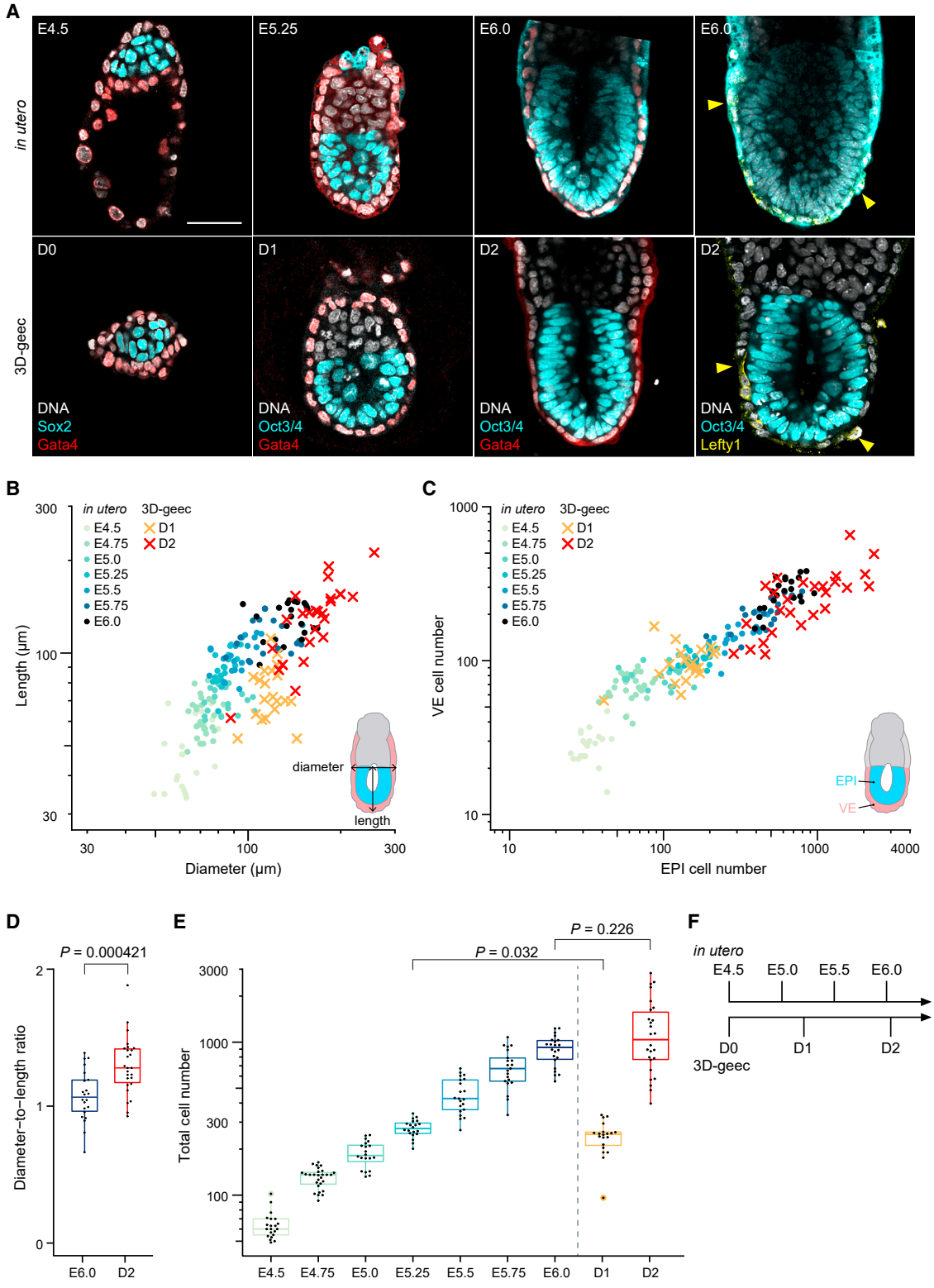

Figure 3. 3D-geec recapitulates *in utero* development from E4.5 to E6.0 by 48 h

(A) Comparison of 3D-geec embryos from day 0 (D0) to 2 (D2; bottom) with embryos developed *in utero* from E4.5 to E6.0 (top). Immunofluorescence images of a representative embryo (see Figure S3 for additional stages) stained for Sox2$^+$ or Oct3/4$^+$ EPI, Gata4$^+$ VE, and asymmetrically localized Lefty1$^+$ AVE (yellow arrowheads).

(legend continued on next page)

of E4.5 embryos developed into an egg cylinder after 48 h in 3D-geec. Collectively, these quantitative control measures (see Figures S2I–S2L; STAR Methods) indicate that 3D-geec recapitulates mouse peri- and post-implantation development to E6.0 with an overall success rate of 49% (Figure 4D).

Live imaging with an inverted light-sheet microscope reveals cellular dynamics

Next, we aimed to develop *in toto* live-imaging microscopy compatible with 3D-geec. Increasing embryo size, photo-sensitivity, and the long gel-filled distance between the imaging objective and the embryo render our system incompatible with most conventional microscopes. We therefore employed an inverted light-sheet microscope (Strnad et al., 2016) to live-image 3D-geec embryos (Figure 5). The mTE-removed E4.5 embryos were embedded in gel, submerged in IVC medium, and further covered by mineral oil to prevent evaporation (Figure 5A). This setting allows for successful live-imaging of mouse peri- and post-implantation embryos under 3D-geec for 48 h without compromising embryonic development, as judged from AVE formation, embryo dimensions, and cell number (Figures 5B–5G; Videos S3 and S4).

Quantitative analysis of cellular dynamics is essential for mechanistic understanding of embryonic morphogenesis and patterning. However, available studies so far have limited their analyses to nuclear tracks and lineages (Ichikawa et al., 2013; McDole et al., 2018; Udan et al., 2014; Yue et al., 2020). To extend the analysis to cell shape changes and cell-cell interactions, we developed a machine-learning-based image-processing pipeline for automatic segmentation of EPI cells based on their plasma membrane signal (Figures 6A and 6B; Video S5). We focused on the first 24 h of the 3D-geec culture until the embryo forms a pro-amniotic cavity to quantitatively analyze cellular dynamics of the EPI tissue both at the level of overall (Figures 6C–6E and S4G–S4I) and single-cell lineages (Figures 6F–6H, S4A–S4F, and S4J–S4L). Whereas cell volume exhibits a regular change at each cell cycle (Figures 6C, 6F, S4A, S4D, S4G, and S4J), many EPI cells undergo elongation, and those elongated cells progressively align radially to form a rosette (Figures 6D, 6E, 6G, 6H, S4B, S4C, S4E, S4F, S4H, S4I, S4K, and S4L). The apical domain emerges in EPI cells and progressively clusters at the center of the EPI tissue as cells elongate, where the pro-amniotic cavity eventually forms (Figures 6L, 6M, and S4M; Video S6). Notably, neighboring cells, but not necessarily cells in the same lineage, become progressively correlated in aspect ratio and alignment, pointing to potential cell-cell interactions assisting in the organization of the EPI tissue (Figures 6I, 6J, and 6K). Together, quantitative characterization of cellular geometry and polarization reveals their dynamic coordination, suggesting feedback mechanisms underlying maturation of the EPI, in addition to the key role that EPI cell polarization plays in pro-amniotic cavity formation (Bedzhov and Zernicka-Goetz, 2014; Christodoulou et al., 2018).

ExE invagination and growth facilitate EPI growth, morphogenesis, and patterning

Whereas the collective behavior of EPI cells may thus drive rosette formation, we noted that EPI cell-cell rearrangement is enhanced upon invagination of pTE cells (Figure S5A). This suggests possible influence by the neighboring ExE tissue on patterning the EPI. To investigate the impact of ExE on EPI growth, morphogenesis, and patterning, we compared cellular dynamics and morphogenesis between 3D-geec embryos with (see Figure 1) and without mTE (see Figures 2, 3, 4, 5, and 6). As described earlier, the latter recapitulates ExE formation in a manner comparable to *in utero* development, whereas the former fails to form the ExE, as pTE cells do not invaginate and instead remain a single layer of cells surrounding the EPI (Figure 7A; see also Figure 1A at 6 and 24 h, and 3A at D1). When cell numbers are compared after 18 h of culture, a properly formed ExE has a higher mean cell number than a pTE that failed to invaginate. Furthermore, the EPI consists of a significantly higher number of cells in the presence of an ExE (Figure 7B). These data suggest that the presence of the neighboring ExE tissue may facilitate growth of the EPI.

To investigate the possible mechanism of this tissue-tissue interaction, we first examined the role of biochemical signaling pathways. Specifically, the expression of Id1 and live-reporter expression of A_7-Venus and Dusp4-T2A-mVenus were used to examine BMP, Nodal-Foxh1 (Takaoka et al., 2017), and FGF-Dusp4 signaling pathways, respectively. Nodal signaling in the EPI exhibits cell-to-cell heterogeneity regardless of the presence of ExE (Granier et al., 2011; Figure S5B). Id1 expression is enriched in the EPI region in contact with the ExE or pTE, regardless of EPI geometry or the presence of ExE (Figure 7C), strongly suggesting that BMP is secreted from the ExE or pTE to activate BMP-Id1 signaling in the proximal EPI, as reported for BMP4 signaling at later stages (Winnier et al., 1995). In marked contrast, FGF-Dusp4 signaling shows an activity gradient across the proximal-distal axis in the EPI, and this patterned signaling activity is lost in the absence of ExE (Figures S5C and S5D). This indicates an essential role for ExE in establishing the FGF signaling landscape in the EPI (Figure 7D). Collectively, these data suggest that biochemical signaling from the ExE acts paracrine to the neighboring EPI tissue to drive its growth and patterning.

Next, we investigated the possibility of mechanical influence of the ExE tissue on the EPI. We noted that a flat or convex boundary forms between the ExE and EPI tissues during pTE invagination and ExE growth (see Figures 3A, 5B, 6B, 7A, 7C, 7D, and S5A). This is in contrast with development without ExE, in which the EPI is surrounded by a single layer of pTE cells. The boundary between ExE and EPI lacks Collagen IV and is

(B and C) Scatterplots showing the length against diameter (B), and cell numbers of PrE/VE covering EPI against EPI (C) for 3D-geec and *in utero* embryos in log scale.
(D) The diameter-to-length ratio for embryos shown in (B).
(E) The total (EPI and PrE/VE) cell numbers for embryos shown in (C).
(F) Scaled timeline of 3D-geec development based on the total cell numbers (E). 3D-geec embryos correspond to E5.20 and E6.04 *in utero* embryos after 24 and 48 h in culture, respectively. n = 21 (E4.5), 28 (E4.75), 20 (E5.0), 20 (E5.25), 21 (E5.5), 21 (E5.75), 22 (E6.0), 20 (D1), and 26 (D2).
p values calculated using t test (D) and Kruskal-Wallis ANOVA followed by multiple Mann-Whitney U test (E). Scale bars, 50 μm. See also Figures S2 and S3.

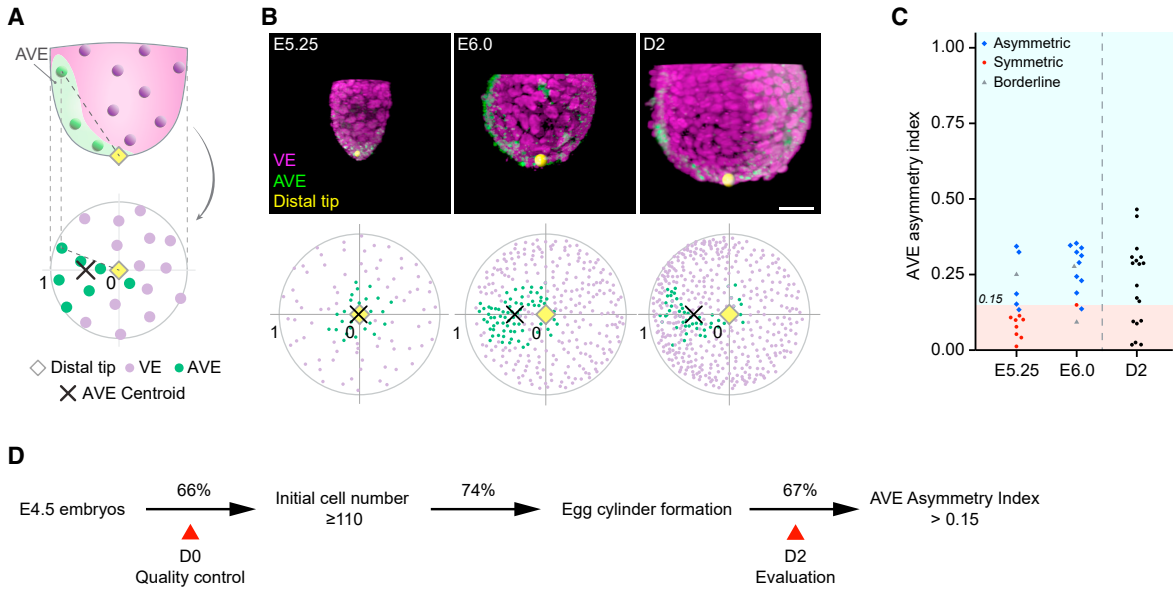

Figure 4. Quantitative evaluation of 3D-geec outcome based on AVE asymmetry at D2

(A) Schematic to calculate the AVE asymmetry index. A polar plot shows the distribution of VE and AVE cells in the embryo, using the distance and angle from the distal tip. The AVE asymmetry index is calculated based on the position of AVE centroid in this polar plot.

(B) Representative 3D projections of E5.25, E6.0, and D2 embryos immunostained for Gata4 (VE) and Lefty1 or Cerl1 (AVE), and their respective polar plots.

(C) AVE asymmetry index of E5.25, E6.0, and D2 embryos. AVE position of *in utero* embryos was first qualitatively classified as asymmetric (blue), symmetric (red), or borderline (gray). No embryos at E5.25 and E6.0 that were classified as symmetric have an AVE asymmetry index larger than 0.15. Thus, we used this value to evaluate 3D-geec D2 embryos for AVE asymmetry. n = 15 (E5.25), 13 (E6.0), and 18 (D2).

(D) Summary of 3D-geec efficiency based on quantitative quality control and evaluation.

Scale bars, 50 μm. See also Figure S2.

therefore distinct from the remainder of the EPI boundary that is enriched with Collagen IV. The presence of Collagen IV enables Integrinβ1-mediated adhesion at the basal side of EPI cells (Bedzhov and Zernicka-Goetz, 2014; Figure 7E). We therefore investigated whether this Collagen-free ExE-EPI boundary impacts the self-organization of the EPI tissue, particularly the formation of the pro-amniotic cavity.

We started with a theoretical analysis of the mechanics to delineate the conditions under which the cavity can achieve stable growth (STAR Methods). Lumen formation has been described as a process analogous to the nucleation of a droplet in a new phase (Duclut et al., 2019). Briefly, lumina may grow if the inner pressure P_L acting on the lumen-tissue interface is large enough to overcome the resisting interfacial tension:

$$\alpha \frac{dR}{dt} = P_L - \frac{2\gamma}{R}.$$

Here, R denotes the lumen radius, α is a dissipative coefficient, and γ is the effective surface tension associated with the lumen-tissue interface. Notably, the resisting surface term scales inversely with the lumen radius; consequently, the size and shape of a lumen determine its growth. Lumina may grow only if their radii exceed the critical threshold $R_{crit} = 2\gamma/P_L$, which is set by the competition of surface and bulk terms. Interestingly, in many physical systems, heterogeneous nucleation—where an external wall or an impurity provides an additional interface for newly forming droplets—dominates over homogeneous nucleation. It is an everyday observation that gas bubbles first form at the surface of a pot of water about to boil. Indeed, the radius of curvature of a nascent droplet adhered to a surface is larger compared with a non-adherent droplet of equal volume (Figures 7F and 7G). Correspondingly, the surface term resisting nucleation is lowered for an adherent droplet (Turnbull, 1950). We hypothesized that the neighboring ExE tissue provides an interface with properties facilitating lumen formation, analogous to heterogeneous nucleation. Assuming that the interfacial tension between the lumen and EPI cells is similar to that between the lumen and the ExE, heterogeneous nucleation may occur as long as the ExE-EPI boundary has a positive interfacial tension. We calculated the parameter regimes in which stable lumen expansion is achieved, and found that our theory predicts more robust lumen formation in the presence of the ExE-EPI boundary (Figure 7H).

To test this prediction, we examined the formation of the pro-amniotic cavity in the embryo developing in the presence or absence of the neighboring ExE tissue. More than half (7 of 13) of the embryos developing with an ExE formed a pro-amniotic cavity after 18 h of 3D-geec, comparable with the 7 of 13 *in utero* developed E5.0 embryos that had a pro-amniotic cavity (Figure 7I). In contrast, the EPI is disorganized in embryos that failed to form an ExE, which is marked by multiple rosettes without a lumen. Regarding the positioning of the nascent pro-amniotic cavity, 38 (90%) of 42 embryos developed in 3D-geec formed the pro-amniotic cavity at the boundary between EPI and ExE tissues (see Figures 5B, 6B, and 7I). Of 36 embryos developed *in utero* (those with a nascent lumen at E4.75, E5.0, and

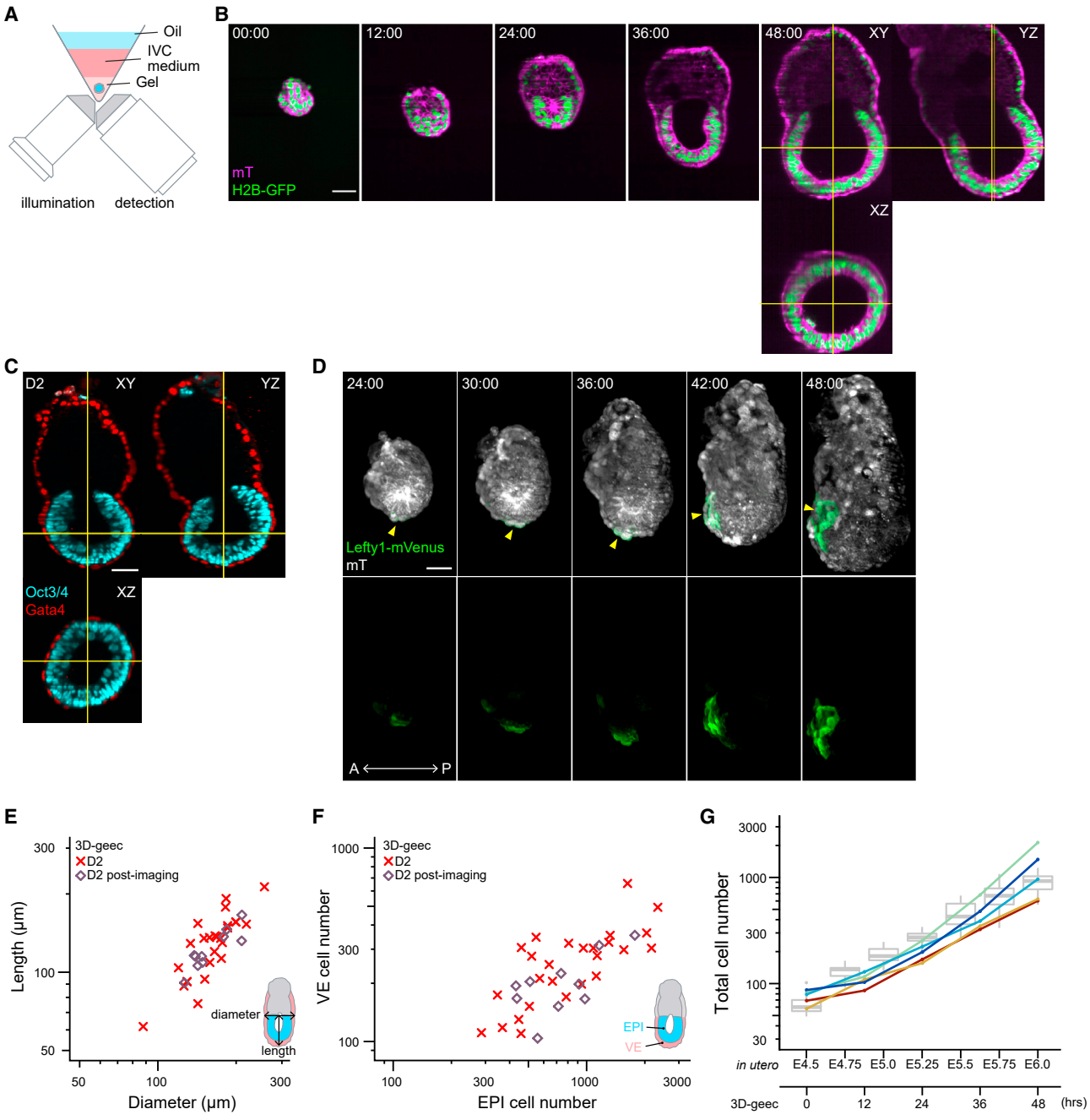

Figure 5. Live-imaging of mouse peri-implantation development during 3D-geec

(A) Design schematic of an inverted light-sheet microscope adapted to 3D-geec.

(B) Time-lapse images of a representative H2B-GFP;mT mouse embryo developing from E4.5 (t = 00:00, hours:minutes) in 3D-geec with inverted light-sheet microscopy. n = 13.

(C) Immunofluorescence of a representative mouse embryo after 48 h 3D-geec live-imaging (B), stained for Oct3/4^{+} EPI and Gata4^{+} VE. n = 10.

(D) Time-lapse images of a representative Lefty1-mVenus;mT embryo developing in 3D-geec during D1 and D2. Arrowheads indicate Lefty1^{+} DVE/AVE cells. n = 5.

(E and F) Embryo dimension (E) and cell number (F) after 48 h 3D-geec live-imaging. There is no significant difference between live-imaged embryos (n = 10) and embryos cultured in the incubator (n = 26, see Figure 3) in terms of diameter (p = 0.899), length (p = 0.475), EPI cell number (p = 0.689), and VE cell number (p = 0.158).

(G) Total cell numbers of live-imaged 3D-geec embryos (line graphs) in comparison with total cell numbers of *in utero* embryos shown in Figure 3E (boxplots). n = 5 (live-imaged).

p values calculated using Mann-Whitney U test (diameter and length in E) and t test (EPI and VE cell number in F). Scale bars, 50 μm. See also Videos S3 and S4.

Developmental Cell
Resource
CellPress OPEN ACCESS

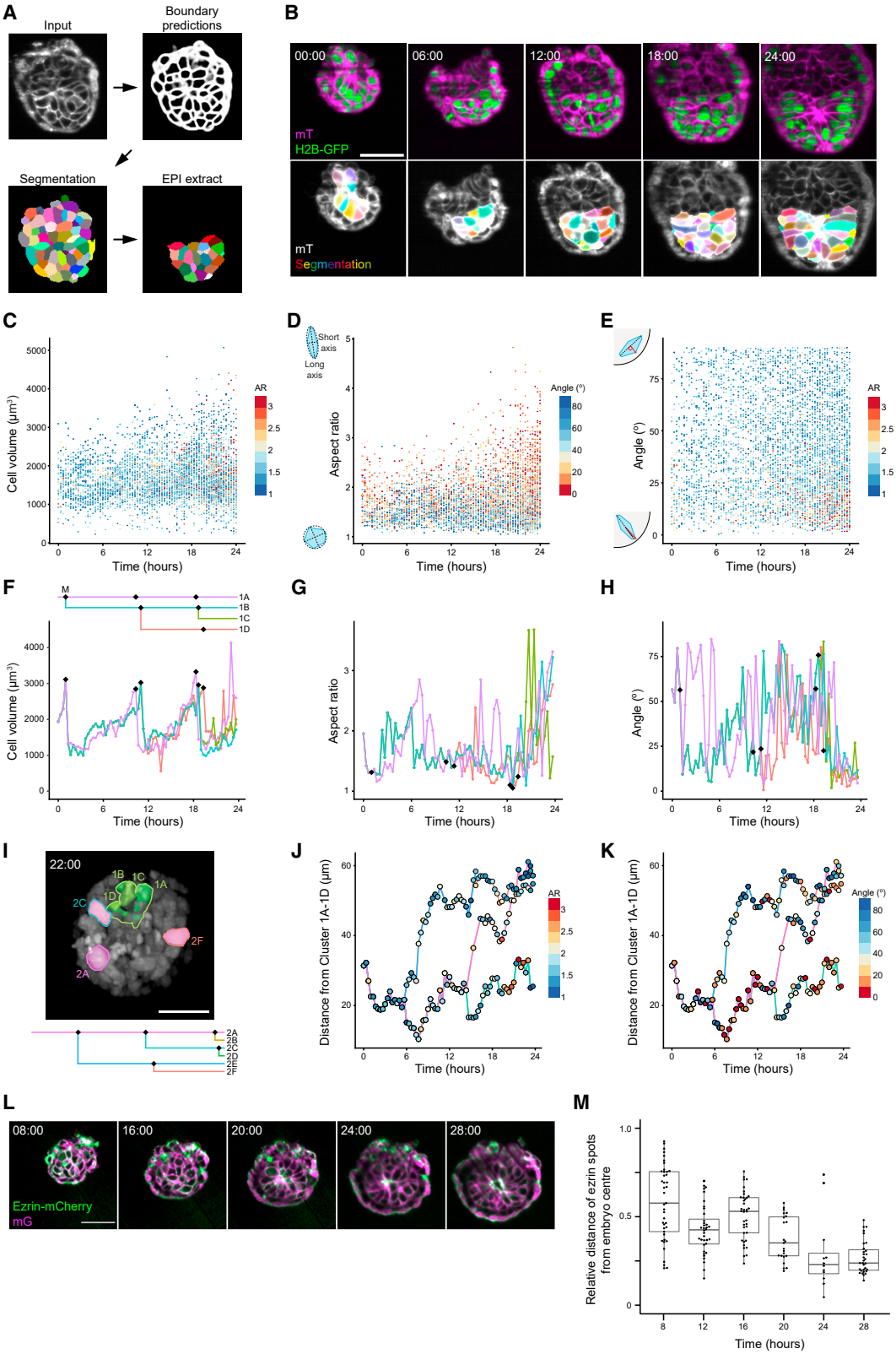

(legend on next page)

E5.25), 24 (67%) formed the pro-amniotic lumen at the boundary between EPI and ExE tissues (Figure S5E), with an additional 4 embryos that had already begun EPI elongation with the lumen connected to the boundary as a fissure-like structure (Figure 7I; a total of 28 embryos, 78%). Furthermore, time-lapse images of 3D-geec embryos show that the lumen emerges at the ExE-EPI boundary (Figure 7J), or alternatively, that while rosettes form at multiple locations within EPI tissue, the lumen expands from the ExE-EPI boundary (Figures S5F and S5G). These data are all in agreement with our calculated prediction that lumen formation is more stable at the ExE-EPI tissue boundary, illustrating the mechanical contribution of the ExE in shaping the EPI.

Taken together, these findings strongly suggest that the ExE acts both biochemically and mechanically on the neighboring EPI to facilitate its growth, morphogenesis, and patterning, leading to EPI elongation and ultimately egg cylinder formation.

DISCUSSION

The new 3D-geec methods presented here enable 3D culture and live-imaging of mouse peri- and post-implantation embryos from E4.5 to E6.0 *ex vivo* over 48 h. A number of quantitative measures, newly introduced for mouse peri-implantation embryos, ensure an efficient success rate and reproducibility. Our findings show that 3D gel culture recapitulates *in utero* development more faithfully than available 2D methods, in line with a recent study that developed human peri-implantation embryo culture in 3D (Xiang et al., 2020). These 3D gel cultures effectively prevent disruption of embryonic morphogenesis, which has been largely inevitable in the 2D culture methods. Our 3D culture method is also compatible with live-imaging using commercially available light-sheet microscopes (Serra et al., 2019; Strnad et al., 2016), offering sufficient spatiotemporal resolution for automatic image analyses, including cell tracking and membrane segmentation. Notably, these microscopes also accommodate multi-sample imaging and enable spatiotemporally controlled perturbations such as photo-manipulation. The unprecedented access to cellular dynamics during peri-implantation development and the capability for *in toto* monitoring, measurement, and manipulation will ultimately lead to finer mechanistic understanding of this crucial period in mammalian development.

In this study, we found that releasing TE tension enables pTE cells to invaginate by apical constriction and proliferate to form the ExE. This ExE in turn facilitates the growth and morphogenesis of the neighboring EPI by establishing BMP and FGF signaling landscapes, consistent with the essential role of BMP signaling in maintaining EPI pluripotency (Di-Gregorio et al., 2007). The reduced growth of EPI in the absence of ExE might also be explained by the role of proprotein convertases, Spc1 and Spc4, secreted by ExE, in activating Nodal signaling in the EPI (Beck et al., 2002). Furthermore, theoretical analysis and biological experiments consistently show that juxta-positioning of the ExE tissue also facilitates luminogenesis and patterned morphogenesis of the EPI tissue. In addition to the direct mechanical effect of the ExE interface, lumen positioning might be facilitated by the radial organization of polarizing EPI cells. This is in line with the findings that whereas embryonic stem cells (Bedzhov and Zernicka-Goetz, 2014) and embryos lacking an ExE (Figures 1, 7, and S5C and S5D) may form rosettes or a pro-amniotic cavity in a simplified geometry, EPI patterning occurs more consistently and robustly *in vivo* through tissue-tissue interactions.

Overall, our data demonstrate the biochemical and mechanical roles of extra-embryonic tissues in mammalian embryonic development, in addition to their impact on VE morphogenesis, which was reported in a recent study (Christodoulou et al., 2019). As the EPI is known to control the proliferation of the ExE via FGF (Christodoulou et al., 2019; Gardner et al., 1973), our findings suggest that reciprocal interactions between embryonic and extra-embryonic tissues (Brennan et al., 2001) start as early as E5.0.

Limitations of the study

Although 3D-geec offers novel access to mouse peri-implantation development, it also leaves us with new challenges. First, the present methods require removal of the mTE, similar to 2D methods (Bedzhov et al., 2014), to release TE tension and to induce formation of the ExE. Whereas this results in robust *ex vivo* recapitulation of mouse peri- and post-implantation development from E4.5 to E6.0 in 3D gel, *in utero* development certainly involves the mTE, which together with the parietal endoderm forms Reichert's membrane (Salamat et al., 1995). When the invasive behavior of mTE cells was experimentally induced by adhesive beads, pTE cells showed constriction with actin enriched at the apical surface, similar to the embryos developed *in utero* (see Figure 1D), suggesting the role of embryo-uterine interaction in tension release (Figures S5H–S5K). However, the exact mechanism of how the TE tension is released

Figure 6. Cellular dynamics underlying mouse peri-implantation morphogenesis and patterning

(A) Schematic explaining the machine-learning-based image-processing pipeline for cell membrane segmentation.

(B) Time-lapse images of a representative H2B-GFP;mT mouse embryo developing during the first 24 h in 3D-geec (top, Figure 5B) and the outcome of automatic cell membrane segmentation (bottom). n = 7.

(C–E) Measurement of volume (C), aspect ratio (D), and long-axis radial alignment against the outer embryonic surface (E) of all EPI cells in a representative embryo (B). Cells are analyzed every 20 min for 24 h of 3D-geec until pro-amniotic cavity formation. n = 2 embryos.

(F–H) Measurement of volume (F), aspect ratio (G), and long-axis radial alignment against the outer embryonic surface (H) of EPI cells in a representative lineage. Black diamonds in a lineage tree and in plots represent mitoses. Non-tracked daughter cells are not shown in the lineage tree. n = 18 lineages.

(I) Cells from the lineage shown in (F–H) (green, Cells #1A–1D) and a different lineage (pink, Cells #2A, 2C, and 2F, also shown in Figures S4A–S4C). Cell #2C (blue-green surface) is in contact with a cluster of cells #1A–1D, while cell #2A (pink) and #2F (red) are distant.

(J and K) Distance between cells in the cluster #2 and the centroid of the cluster #1, with aspect ratio (J) and radial alignment (K) values shown in colors.

(L) Time-lapse images of a representative Ezrin-mCherry;mG mouse embryo developing during the first 28 h in 3D-geec until pro-amniotic cavity expansion. n = 8.

(M) Relative distance of the Ezrin signal from the embryo center in embryos shown in (L).

Scale bars, 50 μm. See also Figure S4 and Videos S5 and S6.

Developmental Cell
Resource
CellPress OPEN ACCESS

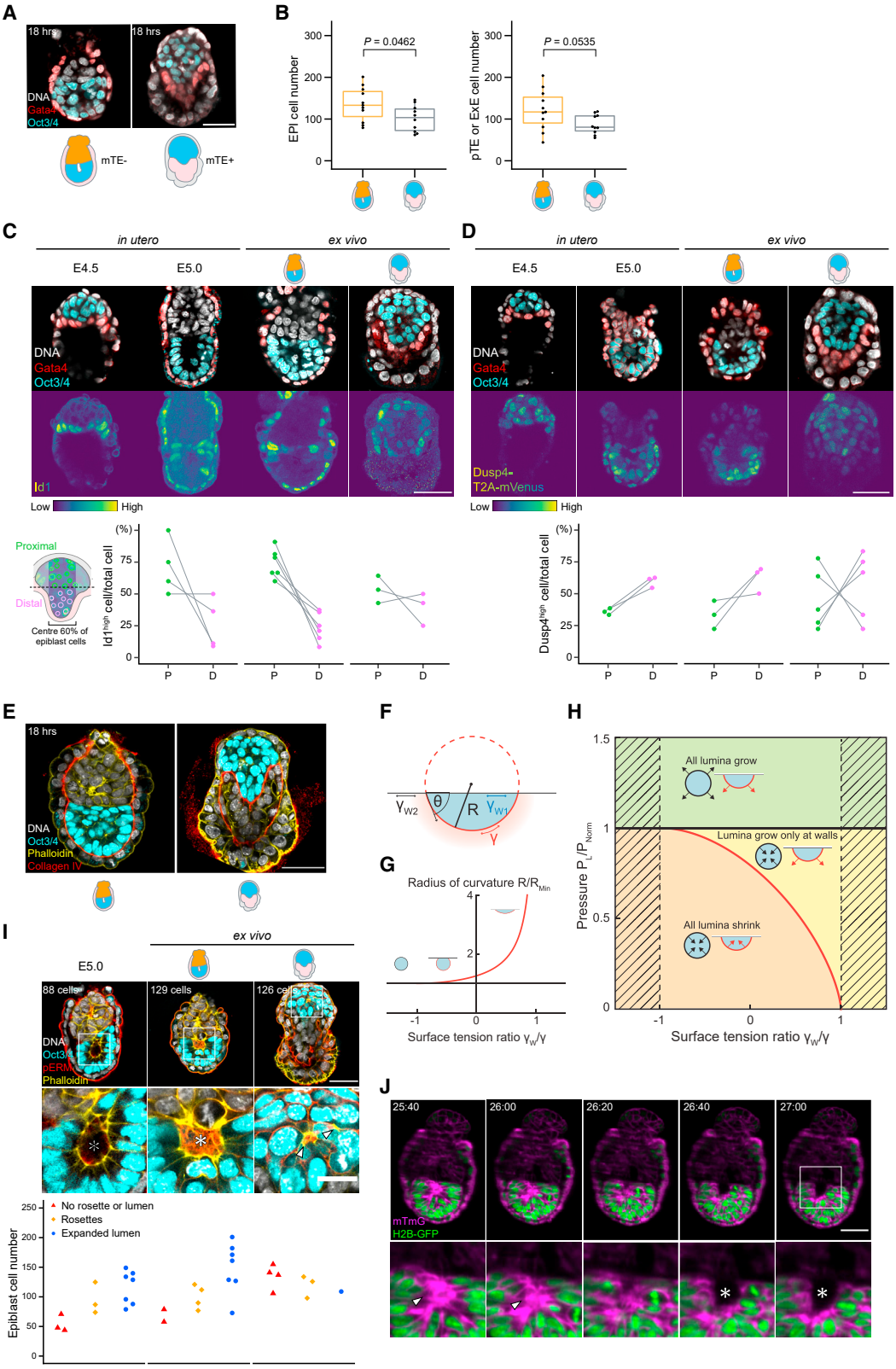

Figure 7. ExE invagination facilitates EPI growth, morphogenesis, and patterning

(A) Immunofluorescence of representative embryos developed *ex vivo* for 18 h from E4.5 in the presence (left) or absence (right) of ExE (hence, in the absence or presence of mTE, respectively), stained for Oct3/4$^+$ EPI and Gata4$^+$ VE.

(legend continued on next page)

in utero and the development of an *ex vivo* culture method that retains the mTE will be topics of future studies. Second, *in utero* development to E4.5 blastocyst is necessary for the high success rate of *ex vivo* culture shown in this study (Figures S2A–S2H). This indicates an as-yet uncharacterized chemical or mechanical role of the uterine environment in the blastocyst maturation and currently precludes the *in vitro* culture of mouse embryos from the zygote through to the post-implantation stage. Finally, the diameter of the 3D-geec embryo is wider than embryos developed *in utero* (Figure 3B). This spherical tissue dimension may be driven by pressurized expansion of the pro-amniotic cavity, similar to blastocyst cavity expansion prior to implantation (Chan et al., 2019; Dumortier et al., 2019; Leonavicius et al., 2018; Niwayama et al., 2019). Moreover, uterine tissue may be necessary to confine this expansion for precise EPI elongation during *in utero* development.

In all cases, it is highly conceivable that mammalian peri- and post-implantation development requires intimate interactions between embryos and extra-embryonic tissues, as well as a contribution from uterine tissues. Further development of methods to recapitulate these interactions *ex vivo*, or to study embryonic development *in situ* inside the uterus (Huang et al., 2020), will be necessary to integrate their respective roles and gain a comprehensive understanding of mammalian development.

STAR★METHODS

Detailed methods are provided in the online version of this paper and include the following:

- KEY RESOURCES TABLE
- RESOURCE AVAILABILITY
  - Lead contact
  - Materials availability
  - Data and code availability
- EXPERIMENTAL MODEL AND SUBJECT DETAILS
  - Animal work
  - Mouse lines and genotyping
  - Mouse embryos
- METHOD DETAILS
  - 3D-gel embedded embryo culture (3D-geec)
  - Cortical tension measurement
  - Immunofluorescence staining and imaging
  - Confocal live-imaging
  - Light-sheet live-imaging
  - Laser ablation with light-sheet live-imaging
  - Blastocyst immunosurgery and culture
  - Microbeads embedding
  - Nucleation theory of lumen formation: Heterogeneous versus homogeneous case
- QUANTIFICATION AND STATISTICAL ANALYSIS
  - Image analysis
  - Machine-learning-based segmentation and analysis
  - Derivation of optimal initial cell number threshold
  - Statistical analysis and data reproducibility
  - Analytical calculations

SUPPLEMENTAL INFORMATION

Supplemental information can be found online at https://doi.org/10.1016/j.devcel.2021.12.023.

ACKNOWLEDGMENTS

We are grateful to the members of the Hiiragi laboratory for discussions and comments on the manuscript, in particular to Prachiti Moghe and Chii Jou Chan for instructing on cortical tension measurement; Ramona Bloehs, Stefanie Friese, and Lidia Pérez for their technical support; and the EMBL animal facility for their support. We thank Jérôme Collignon, Aissam Ikmi, Tristan Rodriguez, and Pamela Carolina Guruciaga for critical reading of the manuscript; Hiroshi Hamada and Katsuyoshi Takaoka for Lefty1-mVenus and A_7-Venus mouse lines; Robert S. Adelstein for GFP-Myh9 mouse line; Daniel Messerschmidt for peri-implantation embryo recovery expertise; and Luxendo for their technical support in light-sheet microscopy and laser ablation. T.I. is supported by JSPS Overseas Research Fellowship, H.T.Z. by the A*STAR National Science Scholarship (NSS PhD), and D.F. by fellowships from the EMBL Interdisciplinary Postdoc Program (EIPOD) under Marie Sklodowska-Curie Actions (COFUND III RTD). The Hiiragi laboratory is supported by EMBL, the European Research Council (ERC Advanced Grant "SelforganisingEmbryo," grant agreement 742732) and JSPS KAKENHI grant number JP21H05038.

(B) EPI cell numbers (left) and pTE/ExE cell numbers (right) in embryos shown in (A). n = 19 and 23, respectively.
(C) Immunofluorescence of representative embryos developed *in utero*, or *ex vivo* for 18 h in the presence or absence of ExE, stained for Id1, Oct3/4$^+$ EPI, and Gata4$^+$ VE. Percentage of Id1^{high} cells in proximal (P) and distal (D) halves of EPI of each embryo. n = 4, 16, 10, and 14, respectively.
(D) Immunofluorescence of representative Dusp4-T2A-mVenus embryos developed *in utero*, or *ex vivo* in the presence or absence of ExE, stained for Oct3/4$^+$ EPI and Gata4$^+$ VE. Percentage of Dusp4^{high} cells in proximal (P) and distal (D) halves of EPI of each embryo. n = 4, 5, 6, and 6, respectively.
(E) Immunofluorescence of representative embryos developed *ex vivo* for 18 h from E4.5 in the presence (left) or absence (right) of ExE stained for Collagen IV, actin, and Oct3/4$^+$ EPI.
(F) Theoretical analysis of lumen formation as a nucleation process. The contact angle θ of a lumen in contact with an external tissue is governed by the surface tensions γ, γ_{W1}, γ_{W2} associated with the different interfaces, as described by Young's equation (see STAR Methods).
(G) The radius of curvature of a lumen in contact with a wall (red line) is always larger than the radius of curvature of a spherical (homogeneous) lumen of the same volume (black line). R_{Min} refers to the radius of the minimal initial spherical lumen of volume V. For $\gamma_W/\gamma < -1$ (in which $\gamma_W = \gamma_{W2} - \gamma_{W1}$), a contact area between lumen and wall is not favored (zero wetting), whereas for $\gamma_W/\gamma > 1$, lumina would undergo complete spreading along the wall (total wetting).
(H) The state diagram shows the parameter regions in which lumina grow or shrink. In the green area, both homogeneous and heterogeneous nucleation events lead to lumen expansion. In the yellow region, only heterogeneous nucleation leads to lumen growth. In the orange region, no lumen growth can be sustained. The hatched regions are outside the regime of partial wetting, where heterogeneous nucleation cannot occur. $P_{Norm} = 2\gamma/R_{Min}$.
(I) Immunofluorescence of representative embryos developed *in utero*, or *ex vivo* for 18 h in the presence or absence of ExE, stained for pERM, actin, and Oct3/4$^+$ EPI. The number of EPI cells in relation to the outcome of EPI patterning (bottom). n = 13, 13, and 8, respectively. Arrowheads and asterisks mark the pERM-enriched rosettes and pro-amniotic cavities, respectively.
(J) Time-lapse images of a representative H2B-GFP;mT mouse embryo developing *ex vivo* in the presence of ExE from E4.5 (t = 00:00, hours:minutes). Arrowheads and asterisks mark rosettes and the pro-amniotic cavity, respectively.
p values calculated using t test. Scale bars, 50 μm or 20 μm (enlarged views). See also Figure S5.

AUTHOR CONTRIBUTIONS

T.I., H.T.Z., and T.H. designed the study; T.I. and H.T.Z. conducted the experiments and analyzed and interpreted the data together with T.H.; L.P. initiated the project and developed an earlier version of the culture methods; A.E. conceived and conducted theoretical analysis; D.F. developed the computational image analysis together with R.S., A.W., and A.K.; E.K. and N.T.-S. generated transgenic mice; L.H. helped with light-sheet microscopy and laser ablation; T.I. and H.T.Z. prepared figures, tables, movies, and methods; and T.H. wrote the manuscript with inputs from all authors.

DECLARATION OF INTERESTS

The authors declare no competing interests.

Received: January 31, 2021
Revised: August 23, 2021
Accepted: December 23, 2021
Published: January 20, 2022

REFERENCES

Arnold, S.J., and Robertson, E.J. (2009). Making a commitment: cell lineage allocation and axis patterning in the early mouse embryo. Nat. Rev. Mol. Cell Biol. *10*, 91–103.

Bailles, A., Collinet, C., Philippe, J.-M., Lenne, P.-F., Munro, E., and Lecuit, T. (2019). Genetic induction and mechanochemical propagation of a morphogenetic wave. Nature *572*, 467–473.

Beck, S., Le Good, J.A., Guzman, M., Haim, N. Ben, Roy, K., Beermann, F., and Constam, D.B. (2002). Extraembryonic proteases regulate Nodal signalling during gastrulation. Nat. Cell Biol. *4*, 981–985.

Bedzhov, I., Leung, C.Y., Bialecka, M., and Zernicka-Goetz, M. (2014). *In vitro* culture of mouse blastocysts beyond the implantation stages. Nat. Protoc. *9*, 2732–2739.

Bedzhov, I., and Zernicka-Goetz, M. (2014). Self-organizing properties of mouse pluripotent cells initiate morphogenesis upon implantation. Cell *156*, 1032–1044.

Biro, M., and Maître, J.-L. (2015). Dual pipette aspiration: a unique tool for studying intercellular adhesion. Methods Cell Biol *125*, 255–267.

Brennan, J., Lu, C.C., Norris, D.P., Rodriguez, T.A., Beddington, R.S.P., and Robertson, E.J. (2001). Nodal signalling in the epiblast patterns the early mouse embryo. Nature *411*, 965–969.

Chan, C.J., Costanzo, M., Ruiz-Herrero, T., Mönke, G., Petrie, R.J., Bergert, M., Diz-Muñoz, A., Mahadevan, L., and Hiiragi, T. (2019). Hydraulic control of mammalian embryo size and cell fate. Nature *571*, 112–116.

Christodoulou, N., Kyprianou, C., Weberling, A., Wang, R., Cui, G., Peng, G., Jing, N., and Zernicka-Goetz, M. (2018). Sequential formation and resolution of multiple rosettes drive embryo remodelling after implantation. Nat. Cell Biol. *20*, 1278–1289.

Christodoulou, N., Weberling, A., Strathdee, D., Anderson, K.I., Timpson, P., and Zernicka-Goetz, M. (2019). Morphogenesis of extra-embryonic tissues directs the remodelling of the mouse embryo at implantation. Nat. Commun. *10*, 3557.

Copp, A.J. (1979). Interaction between inner cell mass and trophectoderm of the mouse blastocyst. II. The fate of the polar trophectoderm. J. Embryol. Exp. Morphol. *51*, 109–120.

Dard, N., Louvet, S., Santa-Maria, A., Aghion, J., Martin, M., Mangeat, P., and Maro, B. (2001). *In vivo* functional analysis of Ezrin during mouse blastocyst formation. Dev. Biol. *233*, 161–173.

de Medeiros, G., Kromm, D., Balazs, B., Norlin, N., Günther, S., Izquierdo, E., Ronchi, P., Komoto, S., Krzic, U., Schwab, Y., et al. (2020). Cell and tissue manipulation with ultrashort infrared laser pulses in light-sheet microscopy. Sci. Rep. *10*, 1942.

Deglincerti, A., Croft, G.F., Pietila, L.N., Zernicka-Goetz, M., Siggia, E.D., and Brivanlou, A.H. (2016). Self-organization of the *in vitro* attached human embryo. Nature *533*, 251–254.

Di-Gregorio, A., Sancho, M., Stuckey, D.W., Crompton, L.A., Godwin, J., Mishina, Y., and Rodriguez, T.A. (2007). BMP signalling inhibits premature neural differentiation in the mouse embryo. Development *134*, 3359–3369.

Duclut, C., Sarkar, N., Prost, J., and Jülicher, F. (2019). Fluid pumping and active flexoelectricity can promote lumen nucleation in cell assemblies. Proc. Natl. Acad. Sci. USA *116*, 19264–19273.

Dumortier, J.G., Le Verge-Serandour, M., Tortorelli, A.F., Mielke, A., de Plater, L., Turlier, H., and Maître, J.-L. (2019). Hydraulic fracturing and active coarsening position the lumen of the mouse blastocyst. Science *365*, 465–468.

Eiraku, M., Takata, N., Ishibashi, H., Kawada, M., Sakakura, E., Okuda, S., Sekiguchi, K., Adachi, T., and Sasai, Y. (2011). Self-organizing optic-cup morphogenesis in three-dimensional culture. Nature *472*, 51–56.

Gardner, R.L., Papaioannou, V.E., and Barton, S.C. (1973). Origin of the ectoplacental cone and secondary giant cells in mouse blastocysts reconstituted from isolated trophoblast and inner cell mass. J. Embryol. Exp. Morphol. *30*, 561–572.

Granier, C., Gurchenkov, V., Perea-Gomez, A., Camus, A., Ott, S., Papanayotou, C., Iranzo, J., Moreau, A., Reid, J., Koentges, G., et al. (2011). Nodal cis-regulatory elements reveal epiblast and primitive endoderm heterogeneity in the peri-implantation mouse embryo. Dev. Biol. *349*, 350–362.

Guzman-Ayala, M., Ben-Haim, N., Beck, S., and Constam, D.B. (2004). Nodal protein processing and fibroblast growth factor 4 synergize to maintain a trophoblast stem cell microenvironment. Proc. Natl. Acad. Sci. USA *101*, 15656–15660.

Hadjantonakis, A.K., and Papaioannou, V.E. (2004). Dynamic *in vivo* imaging and cell tracking using a histone fluorescent protein fusion in mice. BMC Biotechnol *4*, 33.

Harland, R., and Gerhart, J. (1997). Formation and function of Spemann's organizer. Annu. Rev. Cell Dev. Biol. *13*, 611–667.

Hemberger, M., Hanna, C.W., and Dean, W. (2020). Mechanisms of early placental development in mouse and humans. Nat. Rev. Genet. *21*, 27–43.

Hiramatsu, R., Matsuoka, T., Kimura-Yoshida, C., Han, S.-W., Mochida, K., Adachi, T., Takayama, S., and Matsuo, I. (2013). External mechanical cues trigger the establishment of the anterior-posterior axis in early mouse embryos. Dev. Cell *27*, 131–144.

Hsu, Y.-C. (1971). Post-blastocyst differentiation *in vitro*. Nature *231*, 100–102.

Hsu, Y.-C. (1972). Differentiation *in vitro* of mouse embryos beyond the implantation stage. Nature *239*, 200–202.

Huang, Q., Cohen, M.A., Alsina, F.C., Devlin, G., Garrett, A., McKey, J., Havlik, P., Rakhilin, N., Wang, E., Xiang, K., et al. (2020). Intravital imaging of mouse embryos. Science *368*, 181–186.

Ichikawa, T., Nakazato, K., Keller, P.J., Kajiura-Kobayashi, H., Stelzer, E.H.K., Mochizuki, A., and Nonaka, S. (2013). Live imaging of whole mouse embryos during gastrulation: migration analyses of epiblast and mesodermal cells. PLoS One *8*, e64506.

Le Verge-Serandour, M., and Turlier, H. (2021). A hydro-osmotic coarsening theory of biological cavity formation. PLoS Comput. Biol. *17*, e1009333.

Leonavicius, K., Royer, C., Preece, C., Davies, B., Biggins, J.S., and Srinivas, S. (2018). Mechanics of mouse blastocyst hatching revealed by a hydrogel-based microdeformation assay. Proc. Natl. Acad. Sci. USA *115*, 10375–10380.

Maître, J.-L., Niwayama, R., Turlier, H., Nédélec, F., and Hiiragi, T. (2015). Pulsatile cell-autonomous contractility drives compaction in the mouse embryo. Nat. Cell Biol. *17*, 849–855.

Martin, A.C., Kaschube, M., and Wieschaus, E.F. (2009). Pulsed contractions of an actin-myosin network drive apical constriction. Nature *457*, 495–499.

McDole, K., Guignard, L., Amat, F., Berger, A., Malandain, G., Royer, L.A., Turaga, S.C., Branson, K., and Keller, P.J. (2018). *In toto* imaging and reconstruction of post-implantation mouse development at the single-cell level. Cell *175*, 859–876, e33.

McDole, K., and Zheng, Y. (2012). Generation and live imaging of an endogenous Cdx2 reporter mouse line. Genesis *50*, 775–782.

Morris, S.A., Grewal, S., Barrios, F., Patankar, S.N., Strauss, B., Buttery, L., Alexander, M., Shakesheff, K.M., and Zernicka-Goetz, M. (2012). Dynamics

of anterior-posterior axis formation in the developing mouse embryo. Nat. Commun. *3*, 673.

Münster, S., Jain, A., Mietke, A., Pavlopoulos, A., Grill, S.W., and Tomancak, P. (2019). Attachment of the blastoderm to the vitelline envelope affects gastrulation of insects. Nature *568*, 395–399.

Muzumdar, M.D., Tasic, B., Miyamichi, K., Li, L., and Luo, L. (2007). A global double-fluorescent Cre reporter mouse. Genesis *45*, 593–605.

Nagy, A., Gertsenstein, M., Vintersten, K., and Behringer, R. (2003). Manipulating the Mouse Embryo: A Laboratory Manual (Cold Spring Harbor Laboratory Press).

Niwayama, R., Moghe, P., Liu, Y.-J., Fabrèges, D., Buchholz, F., Piel, M., and Hiiragi, T. (2019). A tug-of-war between cell shape and polarity controls division orientation to ensure robust patterning in the mouse blastocyst. Dev. Cell *51*, 564–574.e6.

Ohnishi, Y., Huber, W., Tsumura, A., Kang, M., Xenopoulos, P., Kurimoto, K., Oleś, A.K., Araúzo-Bravo, M.J., Saitou, M., Hadjantonakis, A.-K., et al. (2014). Cell-to-cell expression variability followed by signal reinforcement progressively segregates early mouse lineages. Nat. Cell Biol. *16*, 27–37.

Pienkowski, M., Solter, D., and Koprowski, H. (1974). Early mouse embryos: growth and differentiation *in vitro*. Exp. Cell Res. *85*, 424–428.

Rossant, J., and Tam, P.P.L. (2009). Blastocyst lineage formation, early embryonic asymmetries and axis patterning in the mouse. Development *136*, 701–713.

Ryan, A.Q., Chan, C.J., Graner, F., and Hiiragi, T. (2019). Lumen expansion facilitates epiblast-primitive endoderm fate specification during mouse blastocyst formation. Dev. Cell *51*, 684–697.e4.

Salamat, M., Miosge, N., and Herken, R. (1995). Development of Reichert's membrane in the early mouse embryo. Anat. Embryol. (Berl) *192*, 275–281.

Saunders, J.W.J., and Gasseling, M.T. (1968). Ectodermal-mesenchymal interactions in the origin of limb symmetry. In Epithelial-Mesenchymal Interactions (Williams and Wilkins), pp. 78–97.

Schindelin, J., Arganda-Carreras, I., Frise, E., Kaynig, V., Longair, M., Pietzsch, T., Preibisch, S., Rueden, C., Saalfeld, S., Schmid, B., et al. (2012). Fiji: an open-source platform for biological-image analysis. Nat. Methods *9*, 676–682.

Serra, D., Mayr, U., Boni, A., Lukonin, I., Rempfler, M., Challet Meylan, L., Stadler, M.B., Strnad, P., Papasaikas, P., Vischi, D., et al. (2019). Self-organization and symmetry breaking in intestinal organoid development. Nature *569*, 66–72.

Shahbazi, M.N., Jedrusik, A., Vuoristo, S., Recher, G., Hupalowska, A., Bolton, V., Fogarty, N.N.M., Campbell, A., Devito, L.G., Ilic, D., et al. (2016). Self-organization of the human embryo in the absence of maternal tissues. Nat. Cell Biol. *18*, 700–708.

Shyer, A.E., Huycke, T.R., Lee, C., Mahadevan, L., and Tabin, C.J. (2015). Bending gradients: how the intestinal stem cell gets its home. Cell *161*, 569–580.

Strnad, P., Gunther, S., Reichmann, J., Krzic, U., Balazs, B., de Medeiros, G., Norlin, N., Hiiragi, T., Hufnagel, L., and Ellenberg, J. (2016). Inverted light-sheet microscope for imaging mouse pre-implantation development. Nat. Methods *13*, 139–142.

Tachi, C. (1992). Partial characterization of macromolecular components in fetal bovine serum required for development of mouse blastocysts cultured *in vitro*. Dev. Growth Differ. *34*, 69–77.

Takaoka, K., and Hamada, H. (2012). Cell fate decisions and axis determination in the early mouse embryo. Development *139*, 3–14.

Takaoka, K., Nishimura, H., and Hamada, H. (2017). Both Nodal signalling and stochasticity select for prospective distal visceral endoderm in mouse embryos. Nat. Commun. *8*, 1492.

Takaoka, K., Yamamoto, M., and Hamada, H. (2011). Origin and role of distal visceral endoderm, a group of cells that determines anterior-posterior polarity of the mouse embryo. Nat. Cell Biol. *13*, 743–752.

Thomas, P., and Beddington, R. (1996). Anterior primitive endoderm may be responsible for patterning the anterior neural plate in the mouse embryo. Curr. Biol. *6*, 1487–1496.

Thomas, P.Q., Brown, A., and Beddington, R.S.P. (1998). Hex: A homeobox gene revealing peri-implantation asymmetry in the mouse embryo and an early transient marker of endothelial cell precursors. Development *125*, 85–94.

Torres-Sánchez, A., Kerr Winter, M., and Salbreux, G. (2021). Tissue hydraulics: physics of lumen formation and interaction. Cells Dev. 203724. https://doi.org/10.1016/j.cdev.2021.203724.

Turnbull, D. (1950). Kinetics of heterogeneous nucleation. J. Chem. Phys. *18*, 198–203.

Udan, R.S., Piazza, V.G., Hsu, C.-W., Hadjantonakis, A.-K., and Dickinson, M.E. (2014). Quantitative imaging of cell dynamics in mouse embryos using light-sheet microscopy. Development *141*, 4406–4414.

van den Brink, S.C., Baillie-Johnson, P., Balayo, T., Hadjantonakis, A.-K., Nowotschin, S., Turner, D.A., and Martinez Arias, A. (2014). Symmetry breaking, germ layer specification and axial organisation in aggregates of mouse embryonic stem cells. Development *141*, 4231–4242.

Wang, H., and Dey, S.K. (2006). Roadmap to embryo implantation: clues from mouse models. Nat. Rev. Genet. *7*, 185–199.

Warmflash, A., Sorre, B., Etoc, F., Siggia, E.D., and Brivanlou, A.H. (2014). A method to recapitulate early embryonic spatial patterning in human embryonic stem cells. Nat. Methods *11*, 847–854.

Winnier, G., Blessing, M., Labosky, P.A., and Hogan, B.L.M. (1995). Bone morphogenetic protein-4 is required for mesoderm formation and patterning in the mouse. Genes Dev *9*, 2105–2116.

Wolny, A., Cerrone, L., Vijayan, A., Tofanelli, R., Barro, A.V., Louveaux, M., Wenzl, C., Strauss, S., Wilson-Sánchez, D., Lymbouridou, R., et al. (2020). Accurate and versatile 3D segmentation of plant tissues at cellular resolution. Elife *9*, 1–34.

Xiang, L., Yin, Y., Zheng, Y., Ma, Y., Li, Y., Zhao, Z., Guo, J., Ai, Z., Niu, Y., Duan, K., et al. (2020). A developmental landscape of 3D-cultured human pre-gastrulation embryos. Nature *577*, 537–542.

Yue, Y., Zong, W., Li, X., Li, J., Zhang, Y., Wu, R., Liu, Y., Cui, J., Wang, Q., Bian, Y., et al. (2020). Long-term, *in toto* live imaging of cardiomyocyte behaviour during mouse ventricle chamber formation at single-cell resolution. Nat. Cell Biol. *22*, 332–340.

Zhang, Y., Conti, M.A., Malide, D., Dong, F., Wang, A., Shmist, Y.A., Liu, C., Zerfas, P., Daniels, M.P., Chan, C.-C., et al. (2012). Mouse models of MYH9-related disease: mutations in nonmuscle myosin II-A. Blood *119*, 238–250.

Zheng, Y., Xue, X., Shao, Y., Wang, S., Esfahani, S.N., Li, Z., Muncie, J.M., Lakins, J.N., Weaver, V.M., Gumucio, D.L., et al. (2019). Controlled modelling of human epiblast and amnion development using stem cells. Nature *573*, 421–425.

STAR★METHODS

KEY RESOURCES TABLE

REAGENT or RESOURCE	SOURCE	IDENTIFIER
Antibodies		
Mouse anti-Cdx2	BioGenex	Cat#AM392; RRID: AB_2650531
Mouse anti-Oct3/4	Santa Cruz Biotechnology	Cat#sc-5279; RRID: AB_628051
Goat anti-Gata4	R&D systems	Cat#AF2606; RRID: AB_2232177
Rabbit anti-Sox2	Cell Signaling Technology	Cat#23064; RRID: AB_2714146
Rabbit anti-Phospho-Myosin Light Chain 2 (Thr18/Ser19)	Cell Signaling Technology	Cat#3674; RRID: AB_2147464
Rabbit anti-Phospho-Ezrin (Thr567)/ Radixin (Thr564)/Moesin (Thr558)	Cell Signaling Technology	Cat#3726; RRID: AB_10560513
Rabbit anti-Collagen IV	Millipore	Cat#AB756P; RRID: AB_2276457
Goat anti-Lefty	R&D systems	Cat#AF746; RRID: AB_355566
Rat anti-Cerberus1	R&D systems	Cat#MAB1986; RRID: AB_2275974
Rabbit anti-Id1	BIOCHECK	Cat#BCH-1/195-14
Donkey anti-goat IgG Alexa Fluor 488	Invitrogen	Cat#A11055; RRID: AB_2534102
Donkey anti-goat IgG Alexa Fluor Plus 680	Invitrogen	Cat#A32860; RRID: AB_2762841
Donkey anti-rabbit IgG Alexa Fluor Plus 488	Invitrogen	Cat#A32790; RRID: AB_2762833
Donkey anti-mouse IgG Alexa Fluor Plus 594	Invitrogen	Cat#A32744; RRID: AB_2762826
Donkey anti-mouse IgG Cy5 AffiniPure	Jackson ImmunoResearch	Cat#715-175-150; RRID: AB_2340819
Donkey anti-rat IgG Cy5 AffiniPure	Jackson ImmunoResearch	Cat#712-175-153; RRID: AB_2340672
Chemicals, peptides, and recombinant proteins		
DMEM, low glucose, pyruvate, no glutamine, no phenol red	Gibco	Cat#11880028
Fetal Bovine Serum	PAA	Cat#A15-080
GlutaMAX	Gibco	Cat#35050061
HEPES	Sigma	Cat#H0887
Penicillin-Streptomycin	Gibco	Cat#15070063
Advanced DMEM/F-12	Gibco	Cat#12634010
global medium	CooperSurgical	Cat#LGGG-050
global w/ HEPES medium	CooperSurgical	Cat#LGGH-050
Matrigel, Growth Factor Reduced	Corning	Cat#356230; lot: 7345012
Rat-tail Collagen I	Corning	Cat#354236; lot: 6053001
Fetal Bovine Serum, Embryonic stem cell–grade	Biosera	Cat#FB1001S
KnockOut Serum Replacement	Gibco	Cat#10828010
Insulin-Transferrin-Selenium-Ethanolamine (ITS-X)	Gibco	Cat#51500056
β-estradiol	Sigma	Cat#E8875
Progesterone	Sigma	Cat#P0130
N -acetyl-L-cysteine	Sigma	Cat#A7250
Hoechst 33342, Trihydrochloride, Trihydrate	Invitrogen	Cat#H21492
Sigmacote	Sigma	Cat#SL2
Paraformaldehyde, EM Grade, Purified	Electron microscopy sciences	Cat#19208
Triton X-100	Sigma	Cat#T8787
Anti-mouse serum antibody produced in rabbit	Sigma	Cat#M5774

(*Continued on next page*)

Continued

REAGENT or RESOURCE	SOURCE	IDENTIFIER
Complement sera from guinea pig	Sigma	Cat#S1639
Donkey serum	Sigma	Cat#D9663
Bovine serum albumin	Sigma	Cat#A9647
DAPI (4',6-Diamidino-2-Phenylindole, Dilactate)	Invitrogen	Cat#D3571
Rhodamine Phalloidin	Invitrogen	Cat#R415
Mineral Oil	Sigma	Cat#M8410
Heparin-Agarose	Sigma	Car#H0402
Experimental models: Cell lines		
R1 ES cells	Christian Klasen, Transgenic Core Facility at the European Molecular Biology Laboratory (EMBL)	N/A
Experimental models: Organisms/strains		
Mouse: (C57BL/6xC3H) F1	Laboratory Animal Resources at EMBL	N/A
Mouse: mTmG: Gt(ROSA) 26Sor$^{tm4(ACTB-tdTomato,-EGFP)Luo}$	The Jackson Laboratory; Muzumdar et al., 2007	Stock#007676; RRID: IMSR_JAX:007676
Mouse: H2B-GFP: Tg(HIST1H2BB/EGFP)1Pa	The Jackson Laboratory; Hadjantonakis and Papaioannou, 2004	Stock#006069; RRID: IMSR_JAX:006069
Mouse: GFP-Myh9: Myh9$^{tm6(EGFP/MYH9)Rsad}$	Zhang et al., 2012	N/A
Mouse: Cdx2-GFP: Cdx2$^{tm1(EGFP)Yxz}$	The Jackson Laboratory; McDole and Zheng, 2012	Stock#018983; RRID: IMSR_JAX:018983
Mouse: Lefty1-mVenus: Tg(Lefty1-mVenus)4Hmd	RIKEN BioResource Research Center; Takaoka et al., 2011	Stock#RBRC04414; RRID: IMSR_RBRC04414
Mouse: A_7-Venus	Laboratory for Animal Resources and Genetic Engineering, RIKEN Center for Biosystems Dynamics Research; Takaoka et al., 2017	N/A
Mouse: Ezrin-mCherry	This study	N/A
Mouse: Dusp4-T2A-3xmVenus	This study	N/A
Oligonucleotides		
See Table S1 for Genotyping Primer List	N/A	N/A
Recombinant DNA		
Plasmid: pTarES-Dusp4-Combo7	Volker Lauschke, Aulehla lab in EMBL	N/A
Plasmid: pTar-Axin2-Combo-3xTag	Jana Kress, Aulehla lab in EMBL	N/A
Plasmid: pTarES-Dusp4-3xmCherry-Neo-3xmVenus	This study	N/A
Plasmid: pRN3-Ezrin-mCherry	Sophie Louvet-Vallée; Dard et al., 2001	N/A
Plasmid: pgk-ATG-FRT2-CAG	Judith Reichmann, Ellenberg lab in EMBL	N/A
Software and algorithms		
R v4.0.3	The R Foundation	https://www.r-project.org/ RRID: SCR_001905
RStudio v1.2.1335	RStudio	https://rstudio.com/ RRID: SCR_000432
ggplot2 v3.3.2	Hadley Wickham	https://ggplot2.tidyverse.org/ RRID: SCR_014601
lsmeans v2.30.0	Russell Lenth	https://cran.r-project.org/web/packages/lsmeans/lsmeans.pdf
OriginPro 2019 v9.6.0	OriginLab	https://www.originlab.com/index.aspx?go=PRODUCTS/Origin RRID: SCR_014212
PlantSeg	Wolny et al., 2020	https://github.com/hci-unihd/plant-seg

(*Continued on next page*)

Continued

REAGENT or RESOURCE	SOURCE	IDENTIFIER
Python 3.8	Python Software Foundation	https://www.python.org/ RRID: SCR_008394
Wolfram Mathematica	Wolfram	https://www.wolfram.com/mathematica/ RRID: SCR_014448
ZEN	Carl Zeiss	https://www.zeiss.com/microscopy/us/products/microscope-software/zen.html RRID: SCR_013672
LuxControl	Luxendo	https://luxendo.eu/
DIKERIA	Biro and Maître, 2015	http://www.matebiro.com/software/dikeria
AxioVision	Carl Zeiss	http://www.usask.ca/biology/scopes/AxioVision%204-7-2%20Takeoff%20Guide.pdf RRID: SCR_002677
Fiji	Schindelin et al., 2012	https://fiji.sc RRID: SCR_002285
Imaris v9.2.1	Bitplane	https://imaris.oxinst.com RRID: SCR_007370
Other		
μ-Slide Angiogenesis Dish	Ibidi	Cat#81506
BD Eclipse Needle	BD	Cat#305757

RESOURCE AVAILABILITY

Lead contact

Further information and requests for resources and reagents should be directed to and will be fulfilled by the lead contact, Takashi Hiiragi (t.hiiragi@hubrecht.eu).

Materials availability

All unique/stable reagents generated in this study are available from the lead contact with a completed Materials Transfer Agreement.

Data and code availability

All datasets/codes generated during this study are available upon request.

EXPERIMENTAL MODEL AND SUBJECT DETAILS

Animal work

All animal work was performed in the Laboratory Animal Resources (LAR) at the European Molecular Biology Laboratory (EMBL) with permission from the Institutional Animal Care and Use Committee (IACUC) overseeing the operation (IACUC number TH11 00 11). LAR is operated according to the Federation of European Laboratory Animal Science Associations (FELASA) guidelines and recommendations. All mice were maintained in specific pathogen-free conditions with 12-12 hours light-dark cycle and used for experiments at the age of 8 to 35 weeks.

Mouse lines and genotyping

The following mouse lines were used in this study: a F1 hybrid strain between C57BL/6 and C3H (B6C3F1) as wild-type (WT), mTmG (Muzumdar et al., 2007), H2B-GFP (Hadjantonakis and Papaioannou, 2004), GFP-Myh9 (Zhang et al., 2012), Cdx2-GFP (McDole and Zheng, 2012), Lefty1-mVenus (Takaoka et al., 2011), and A_7-Venus (Takaoka et al., 2017). Ezrin-mCherry and Dusp4-T2A-3xmVenus were generated in this study. Standard tail genotyping procedures were used to genotype transgenic mice (for primers and PCR product sizes, see Table S1).

To generate Ezrin-mCherry mice, human ezrin coding sequence tagged with mCherry was PCR amplified using pRN3-Ezrin-mCherry plasmid (a gift from Sophie Louvet-Vallée; Dard et al., 2001) as a template and primers introducing Nhe1 and EcoR1 recognition sites at the ends of the amplicon. The PCR fragment was digested with Nhe1 and EcoR1 and then inserted into pgk-ATG-FRT2-CAG plasmid (a gift from Judith Reichmann, Ellenberg lab in EMBL) cut with the same restriction enzymes. The obtained plasmid contained Ezrin tagged with mCherry under CAG promoter. This plasmid was digested with Pvu1, and the resulting 7018 bp fragment was used for pronuclear injection into C57BL/6 zygotes to generate a mouse with random integration.

To generate Dusp4-T2A knock-in alleles, we targeted the stop codon of endogenous Dusp4 locus with one selection and two different reporter cassettes coding for a destabilized triple mCherry and triple mVenus. The reporter cassettes were flanked by loxP- and FRT-sites to remove the selection cassette. Thus, the targeting vector was constructed as follows: *loxP-T2A-3xmCherry-NLS-PEST-FRT-PGK Neo-loxP-T2A-3xmVenus-NLS-PEST-FRT*. Cre-mediated excision resulted in Dusp4-T2A-3xmVenus allele used in this study. Dusp4-T2A-3xmVenus knock-in reporter line was generated by standard gene targeting techniques using R1 embryonic stem cells. Briefly, chimeric mice were obtained by C57BL/6 blastocyst injection and then outbred to establish the line through germline transmission.

Mouse embryos

To obtain mouse embryos, mice were naturally mated, and noon on the day when a vaginal plug was detected was defined as embryonic day 0.5 (E0.5). Recovery of all embryos was performed under a stereomicroscope (Zeiss, StreREO Discovery.V8) equipped with a thermo plate (Tokai Hit) at 37°C. Pre-implantation blastocysts were recovered by flushing dissected oviducts and uteri with global® medium w/ HEPES (LifeGlobal, LGGH-050). Peri- and post-implantation embryos were recovered from dissected uteri in dissection medium (DMEM (Gibco, 11880028) supplemented with 15% heat-inactivated FBS (PAA, A15-080), 2 mM GlutaMAX (Gibco, 35050061), 10 mM HEPES (Sigma, H0887), 25 units/mL Penicillin and 25 μg/mL Streptomycin (Gibco, 15070063)). Blastocysts at E4.5 are either floating in the uterine luminal space or loosely adherent to the uterine luminal epithelium, and can be isolated by opening along with the mesometrial side of the uterus, followed by a gentle touch using fine forceps (Dumont, No.5). Sites of embryo adherence can be identified by locally red and swollen luminal epithelium tissue. Recovery of later post-implantation embryos is as described (Nagy et al., 2003). The Reichert's membrane of the post-implantation embryos was removed using sharp needles (BD eclipse, 305757). Recovered embryos were handled using an aspirator tube (Sigma, A5177) equipped with a glass pipette pulled from glass micropipettes (Blaubrand intraMark 708744) and cultured in an incubator with a humidified atmosphere of 5% CO_2 at 37 °C (Thermo Scientific, Heracell 240i).

METHOD DETAILS

3D-gel embedded embryo culture (3D-geec)

Gel mix for embedding was prepared on ice, first adding basal medium (advanced DMEM/F-12 (Gibco, 12634010) supplemented with 2 mM GlutaMAX, 25 units/mL Penicillin and 25 μg/mL Streptomycin), growth factor reduced Matrigel (Corning, 356230, lot. 7345012), and then rat-tail Collagen I (Corning, 354236, lot. 6053001). Due to lot-to-lot variation of Matrigel and Collagen I, it is recommended to test for culture side-by-side prior to a large purchase. We tested three lots of Matrigel (lot. 7107329, 7202001, and 7543012) and two lots of Collagen I (lot. 5064009 and 6053001) and selected as above based on the rate of successful egg cylinder formation. We also examined different combinations of the final concentration of Matrigel and Collagen I ranging from 0.5 to 5.0 mg/mL and 0 to 0.7 mg/mL, and found 3.0 mg/mL and 0.3 mg/mL resulted in the best performance, respectively. 15 μL gel mix was added in an inner well of the μ-Slide Angiogenesis dish (Ibidi, 81506), and then embryos quickly rinsed with the gel mix were carefully embedded in the gel droplet so that they did neither adhere to the surface of the dish nor float at the interface of the gel. After solidification of the gel upon 30 minutes incubation in the incubator, 50 μL pre-warmed IVC1 medium (Bedzhov et al., 2014) was added to fill the upper well. IVC1 medium was exchanged for IVC2 medium (Bedzhov et al., 2014) after 24 hours of culture.

For 3D gel-embedded embryo culture (3D-geec), mural trophectoderm (mTE) was microsurgically removed from E4.5 embryos immediately after recovery using sharp needles under a stereomicroscope. mTE-removed embryos were then embedded as described above. To count the initial number of cells, mTE-removed embryos were incubated in IVC1 containing 5 μg/mL Hoechst 33342 (Invitrogen, H21492) for 30 minutes at 37°C. Embryos were rinsed with IVC1 three times and live-imaged with 405 nm laser on a confocal microscope (Zeiss, LSM880) in a custom-made incubation box set to 5% CO_2 and 5% O_2 at 37 °C. To minimise the UV-damage, imaging was achieved within 30 seconds by using Airyscan Fast mode. This additional step before culture ensures the highest quality and consistent experimental outcome without compromising the development (Figure S2L).

Cortical tension measurement

Micropipette aspiration set-up was used as described previously (Biro and Maître, 2015; Maître et al., 2015) to measure the cortical tension of pTE cells. Briefly, microforged micropipettes coated with Sigmacote (Sigma, SL2) of radius 3-4 μm were coupled to a microfluidic pump (Fluigent, MFCS-VAC). Pressures were increasingly applied in a step-wise manner, until reaching a cortex deformation which has the radius of the micropipette in use (R_p). At steady state, the cortical tension γ of the pTE is calculated based on Young–Laplace's law: $\gamma = P_c/2(1/R_p - 1/R_c)$, where P_c is the pressure used to deform the cell of radius R_c. Embryos were cultured in suspension by hanging-drop of IVC1 medium for 6 hrs, prior to micropipette aspiration. The surface of the glass-bottom dish was also coated with Sigmacote to prevent the embryos from attachment to the dish. Microscopic inspection of cell membrane deformation ensured aspiration of a single pTE cell.

Immunofluorescence staining and imaging

Embryos were fixed with 4% paraformaldehyde (Electron microscopy sciences 19208) in PBS for 15 minutes (*in utero* developed embryos) or 30 minutes (*ex vivo* cultured embryos) at room temperature and subsequently permeabilized with 0.5% Triton X-100 (Sigma, T8787) in PBS for 30 minutes at room temperature with gentle agitation. Embryos were incubated in blocking buffer (5% donkey serum

(Sigma, D9663), 2.5% BSA (Sigma, A9647), 0.05% Triton X-100 in PBS) overnight at 4°C with gentle agitation. Embryos were then incubated with primary antibodies diluted in the blocking buffer overnight at 4°C or 2 hours at room temperature. After washing with the blocking buffer, embryos were further incubated with secondary antibodies diluted in the blocking buffer for 2 hours at room temperature. Dye staining was simultaneously performed with the secondary antibody staining, using DAPI (Invitrogen, D3571) at 10 μg/mL or Rhodamine Phalloidin (Invitrogen, R415) diluted at 1:400. Finally, stained embryos were mounted in PBS.

Primary antibodies against Oct3/4 (Santa Cruz Biotechnology, sc-5279), Gata4 biotinylated (R&D systems, AF2606), Sox2 (Cell Signaling, 23064), and Cdx2 (Biogenex Laboratories, MU392AUC), and Collagen IV (Millipore, AB756P) were diluted at 1:200. Primary antibodies against di-phosphorylated myosin regulatory light chain (ppMRLC) (Cell Signaling, 3674), and phosphorylated ERM (pERM) (Cell Signaling, 3726) were diluted at 1:100. Primary antibodies against Lefty (R&D systems, AF746), Cerberus1 (R&D systems, MAB1986), and Id1 (Biocheck, BCH-1/195-14) were diluted at 1:50.

Secondary antibodies, donkey anti-goat IgG Alexa Fluor 488 (Invitrogen, A11055), donkey anti-goat IgG Alexa Fluor Plus 680 (Invitrogen, A32860), donkey anti-rabbit IgG Alexa Fluor Plus 488 (Invitrogen, A32790), donkey anti-mouse IgG Alexa Fluor Plus 594 (Invitrogen, A32744), donkey anti-mouse IgG Cy5 AffiniPure (Jackson ImmunoResearch, 715-175-150), donkey anti-rat IgG Cy5 AffiniPure (Jackson ImmunoResearch, 712-175-153) were used at 1:200.

Images of immunostained embryos were obtained by LSM880 equipped with a C-Apochromat 40x/1.2 NA water immersion objective (Zeiss). ASE-YFP and Dusp4-mVenus signals were imaged by LSM confocal mode. Otherwise, Airyscan Fast mode was used, and raw Airyscan images were post-processed by ZEN black software (Zeiss). E6.0 and D2 embryos in Figure 4B, and embryos after 48 hours of live-imaging in Figure 5C were imaged by an inverted light-sheet microscope (Bruker, Luxendo, InVi SPIM) to illuminate in deep.

Confocal live-imaging

After removal of mTE, Cdx2-GFP embryos were mounted in 10 μL IVC1 drops covered with mineral oil (Sigma, M8410) on 35 mm glass-bottom dishes (MatTek, P35G-1.5-14-C). Live-imaging was performed on a confocal microscope (Zeiss, LSM780) equipped with a custom-made incubation box set to 5% CO_2 and 5% O_2 at 37 °C, and a C-Apochromat 40x/1.2 NA water immersion objective. Images were acquired every 5 minutes with 13 Z-slices separated by 5 μm (Figure 1J).

Light-sheet live-imaging

3D-geec embryos were live-imaged using InVi SPIM. Up to ten embryos were embedded in a 10 μL gel mix within the V-shaped sample holder covered with transparent FEP foil, carefully positioned so that they are at proximity but do not attach to the FEP foil which would disrupt morphogenesis via adhesion. After gelification, embryos were immersed in 75 μL IVC1 medium and further covered with 200 μL mineral oil to prevent evaporation. IVC1 medium was exchanged for IVC 2 medium after 24 hours of culture. The sample holder was enclosed in an environmentally controlled incubation box with 5% CO_2 and 5% O_2 at 37 °C.

InVi SPIM was equipped with a Nikon 25x/1.1NA water immersion detective objective and a Nikon 10x/0.3 NA water immersion illumination objective. The illumination plane and focal plane were aligned before each imaging session and maintained during the imaging. Images were taken every 20 min by a CMOS camera (Hamamatsu, ORCA Flash4.0 V2) with line-scan mode in LuxControl (Luxendo). The imaged volume in case of 48 hours of continuous live-imaging was 425.98×425.98×400 μm^3, with a physical voxel size of 0.208×0.208×1.000 μm^3, along the X, Y and Z axis, respectively. For the live-imaging shorter than 24 hours, the volume was 212.99×212.99×200 μm^3 with a physical voxel size of 0.104×0.104×1.000 μm^3. The lasers and filters used were 488 nm and BP525/50, 515 nm and BP545/40, 561 nm and LP561, and 594 nm and BP632/60 to image GFP, mVenus, tdTomato, and mCherry fluorophores, respectively. Exposure time for each plane was set to 50 ms. Eighty-one % (n=13 of 16) embryos that expressed both H2B-GFP and mT, alternatively 77% (n=23 of 30) embryos that expressed mT regardless of H2B-GFP, developed into the egg cylinder after 48 hours of live-imaging from 5 independent experiments (Figure 5B) without substantial change in embryo size and cell number (Figures 5E and 5F), suggesting no significant harmful effects of live-imaging on 3D-geec development.

Laser ablation with light-sheet live-imaging

To perform laser ablation of embryos in gel while light-sheet live-imaging, we equipped InVi SPIM with a photomanipulation module (Bruker, Luxendo) (de Medeiros et al., 2020). Specifically, a pulsed infrared (IR) laser at 1040 nm, 200 femtoseconds pulse length and 1.5W (Spectra-Physics, HighQ-2) was coupled with the detection objective. The illumination spot of IR laser was aligned at the focal plane before each experimental session and maintained during the experiment to ensure spatial control of the ablation while avoiding wound response. Viability of ablated embryos was verified by embryo growth at 6 hours of culture after ablation.

Ablation at the cell-cell junction in a TE layer was performed by defining a circular ROI of 0.8 μm in diameter on the GFP-Myh9 enriched cell-cell junction, and using 100% laser power, 100 ms dwell time, 5 times repetitions and 2 pixels spacing in LuxControl. Images were taken every 15 seconds with 5 Z-slices separated by 1 μm. Only those experiments in which laser ablation did not elicit typical wound responses such as cortex blebbing, cell swelling or bursting were considered for analysis (Figures 1F–1I).

Blastocyst immunosurgery and culture

Blastocysts recovered at E3.5 as described above were treated with 0.5% (w/v) Protease (Sigma, P8811) in an incubator with a humidified atmosphere of 5% CO_2 at 37 °C to remove zona pellucida and subsequently cultured for 24 hours in 2μl global medium (LifeGlobal, LGGG-050) drops under mineral oil on 35 mm glass-bottom dishes (MatTek, P35G-1.5-14-C) treated with Sigmacote. The TE layer was

removed by from blastocysts by immunosurgery (Ohnishi et al., 2014). Briefly, blastocysts were incubated for 30 minutes in anti-mouse serum antibody (Sigma, M5774) diluted 1:3 in global medium at 37 °C, washed in global medium, followed by incubation for 30 minutes in complement sera from guinea pig (Sigma, S1639) diluted 1:3 in global medium at 37 °C. Lysed TE cells were removed by mouth pipetting. As the pTE is more tightly attached to the ICM than the mTE, extensive mouth pipetting resulted in complete TE removal, while gentle mouth pipetting left remnant pTE cells. Embryos were then allowed to recover for 30 minutes in IVC1 medium before being embedded for 3D-geec as described above. Embryos were fixed after 24-28 hours of culture and subjected to immunofluorescence staining and imaging.

Microbeads embedding

Heparin-Agarose microbeads (Sigma, H0402) washed in PBS three times, followed by incubation in 0.1% BSA containing PBS overnight at 4°C with gentle agitation were used to establish adhesive contact with mTE cells. Beads were washed in basal medium to remove excess BSA prior to embedding into gel together with embryos and carefully positioned in proximity to embryos. Embryos were fixed after 18 hours of culture, and only those embryos that adhered to beads retained beads while fixation.

Nucleation theory of lumen formation: Heterogeneous versus homogeneous case

Fluid-filled cavities can appear within cellular assemblies, and such lumina play important roles during embryonic development (Ryan et al., 2019). Lumen formation has been described as a process analogous to the nucleation of a droplet in a new phase (Duclut et al., 2019), where the competition between a surface- and a bulk term sets a critical radius above which a lumen can grow. In many biological systems, active processes contribute to these terms, i.e., cytoskeleton-generated cellular surface tensions and active pumping of fluid by the cells (Torres-Sánchez et al., 2021; Le Verge-Serandour and Turlier, 2021).

In many physical systems, heterogeneous nucleation – where an external wall or an impurity provides an additional interface – dominates over homogeneous nucleation. In classical nucleation theory, this is explained as a lowering of the free energy barrier that needs to be overcome for nucleation when an additional interface lowers the surface energy of the forming droplet (Turnbull, 1950). Here we investigate the role of an additional tissue in lumen formation. The external tissue acts like a wall on which heterogeneous nucleation can occur. We show how the presence of this additional interface facilitates lumen formation.

Critical radius for lumen formation

We begin by deriving the critical radius above which a lumen will expand and below which it will disappear. This radius depends on the parameters of the system, i.e., the lumen pressure and the surface tension associated with the tissue-lumen interface. For a spherical lumen, the balance of forces at each point of the tissue-lumen interface is given by the Young-Laplace equation:

$$P = \frac{2\gamma}{R}, \qquad \text{(Equation 1)}$$

in which P is the pressure difference across the tissue-lumen interface, γ is a positive effective surface tension associated to the tissue-lumen interface, and R is the radius of the lumen. We assume that the pressure equilibrates within the cavity on the timescale of the radius dynamics and can thus be taken to be uniform. In general, P has several contributions, including active pumping terms. We decompose the pressure into a constant term P_L and a dissipative term, and write the following constitutive relation:

$$P = P_L - \alpha \frac{dR}{dt}, \qquad \text{(Equation 2)}$$

in which α is a dissipative coefficient associated with changes of the lumen radius. Here we do not consider any other dependencies of the pressure on the radius. From Equations 1 and 2, we obtain a differential equation for the lumen radius:

$$\alpha \frac{dR}{dt} = P_L - \frac{2\gamma}{R} \qquad \text{(Equation 3)}$$

that has the traditional form of a nucleation equation with competing bulk and surface terms.

The critical radius for lumen growth is given by:

$$R_{crit} = \frac{2\gamma}{P_L}.$$

Whether lumina of a given size will grow or shrink depends on the parameters γ and P_L which are actively regulated by the cells through the formation of their apical domains and their pumping activities. A lumen can expand when the bulk term dominates over the surface term, i.e., when active fluid pumping overcomes the cost of increasing the lumen-cell interface.

Presence of a wall

We assume that the system is able to produce initial proto-lumina with a finite initialization volume V - set for example by a characteristic exocytosis volume. The initial proto-lumen radius for the homogeneous case – i.e., in the absence of a wall – is then given by:

$$R_{Hom} = \sqrt[3]{\frac{3V}{4\pi}}.$$

In classical heterogeneous nucleation, additional interfaces can lower the energetic cost of forming a new droplet interface, thereby reducing the work for nucleating the new phase at the boundary. In this case, a droplet in contact with the wall takes the shape of a spherical cap, for which the volume can be expressed in terms of the radius of curvature R_{Het} and the contact angle θ (Figure 7F):

$$V = \frac{\pi}{3} R_{Het}^3 (2 + \cos\theta)(1 - \cos\theta)^2.$$

The contact angle is modified by the additional interfacial tensions with the wall as given by the Young equation:

$$\cos\theta = \frac{\gamma_{W2} - \gamma_{W1}}{\gamma}.$$

In the following, we denote by $\gamma_W = \gamma_{W2} - \gamma_{W1}$, the difference between the surface tensions associated with the wall-tissue and wall-lumen interfaces. The heterogenous configuration is only favourable when the properties of the wall are such that $-\gamma < \gamma_W < \gamma$, i.e., when the system is in the partial wetting regime. The radius of curvature – which sets the surface term in Equation 3 – is then given by:

$$R_{Het} = \sqrt[3]{\frac{3V\gamma^3}{\pi(\gamma - \gamma_W)^2(2\gamma + \gamma_W)}}.$$

Figure 7G shows how R_{Het} varies as a function of the surface tensions. Note that $R_{Het} > R_{Hom}$. The regimes of growth and shrinkage for the homogeneous and heterogeneous cases are depicted in Figure 7H.

In conclusion, if the interfacial tensions favor the formation of a new interface between the lumen and the wall, lumen expansion is facilitated by the presence of the wall.

Lumen formation in the mouse epiblast

During embryonic development in mouse, a lumen called the pro-amniotic cavity forms within the EPI. The EPI at this stage is adjacent to the ExE (Figure 1A). We hypothesize that the extra-embryonic interface may facilitate luminogenesis in analogy with the mechanism of heterogeneous nucleation. To enable heterogeneous nucleation, the interfacial tensions between ExE, EPI and the nascent lumen would need to fulfil the partial wetting condition $-\gamma < \gamma_{W2} - \gamma_{W1} < \gamma$.

Assuming that the interfacial tension between lumen and EPI is similar to that between lumen and ExE, i.e., that $\gamma \approx \gamma_{W1}$, we find that the condition for complete wetting is $\gamma_{W2} > 2\gamma$. In this regime, lumen-tissue interfaces are strongly favoured over the tissue-tissue interface, and nucleating lumina would completely spread along the tissue boundary. Conversely, the condition for zero wetting is $\gamma_{W2} < 0$, i.e., where the presence of strong adhesion between the tissues renders the surface tension negative. A negative tension at the tissue-tissue interface however would be expected to lead to shape instabilities which are not observed.

If lumina at the interface between the EPI and the ExE reside within the partial wetting regime, their expansion should be facilitated at this boundary. Then, luminogenesis is predicted to occur predominantly adjacent to the extra-embryonic interface, and loss of this interface is expected to disrupt luminogenesis. Our experimental observations agree with these predictions (Figures 7I, 7J, S5F, and S5G).

QUANTIFICATION AND STATISTICAL ANALYSIS

Image analysis

Dimension measurements (Figures 3B, 3D, 5E, S2F, and S2G), cell counts (Figures 3C, 3E, 5F, 5G, 7B, 7I, S2C–S2E, and S2J–S2L), cell coordinates analysis (Figures 4A–4C and S5A) and apical domain detection (Figure 6L and 6M) were performed with Imaris v9.2.1 (Bitplane). Signal intensity measurements (Figures 1D, 7C, 7D, S2H, S5C, S5D, and S5K) and cell shape analysis (Figures 1B, 1G–1I, and S5J) were performed with Fiji (Schindelin et al., 2012). Cell tracking (Figure S5A) was performed with Fiji and Imaris. Whole embryo images were used for E4.5—E5.25 embryos. To compensate for signal attenuation in thicker samples, the half of the egg cylinder closer to the objective were used for dimension measurements and cell counts.

Evaluation of embryo morphology

Dimension measurements of *in utero* and 3D-geec embryos were performed in 3D using Measurement Points. For blastocysts, the diameter is defined as the mean of the long and short transverse axes of the ICM, and the length is defined as the distance between the EPI-pTE boundary and the apical surface of the PrE. For egg cylinders, the diameter is defined as the mean of the long and short transverse axes of the egg cylinder, and the length is defined as the distance between the ExE-EPI boundary and the distal tip of the egg cylinder.

Evaluation of embryo development based on cell numbers

Cell counts of *in utero* and 3D-geec embryos were performed in 3D using automated Spots detection with manual correction. Initial cell number (Figures S2J and S2K) was based on all nuclei stained by Hoechst 33342. VE (Figures 3C and 5F; also Figure 4) is defined as the visceral endoderm overlying EPI; visceral endoderm overlying ExE is excluded from this analysis. Total cell number is defined as the sum of VE and EPI.

To calculate the corresponding "*in utero* age" of D1 and D2 embryos based on their total cell numbers, a linear regression line was generated from the total cell numbers of *in utero* embryos ($y = 75.06e^{0.0712x}$, $R^2 = 0.933$, where y is the total cell number (Figure 3E) and x is the age of the embryo in hours from conception; Figure S3D). Similarly, a linear regression line was generated from the EPI cell

numbers of *in utero* embryos ($y = 36.77e^{0.0818x}$, $R^2 = 0.929$, where y is the EPI cell number (Figure 3C) and x is the age of the embryo in hours from conception; Figure S3E).

Evaluation of cell differentiation and embryo patterning at D2

VE cells were annotated for AVE identity by co-immunostaining of Gata4 and AVE markers, Lefty1 or Cerberus1, and their positions marked using automated Spots detection with manual correction. The distal tip of the egg cylinder was marked manually as a Spots object and set as the origin for the polar and Cartesian plots. A Reference Frame (X, Y, Z) was created with the *Z*-axis aligned along the proximal-distal axis of the egg cylinder. The 3D coordinates of the Spots in the given Reference Frame were used to calculate linear distance from origin r and angle of rotation θ about the *Z*-axis of each VE cell:

$$r = \sqrt{(x^2 + y^2 + z^2)}$$

$$\theta = tan^{-1}\left(\frac{y}{x}\right)$$

where (x, y, z) are the coordinates of the VE cell.

E5.25 and E6.0 embryos were manually classified as Asymmetric, Symmetric or Borderline by qualitative AVE distribution. Polar plots of the spread of VE cells in each E5.25, E6.0 or D2 embryo were generated and converted to Cartesian coordinates, and the centroid of the AVE cells for each embryo was calculated using the Cartesian coordinates. The linear distance of the AVE centroid from the origin r_{cent}, scaled to the largest VE linear distance of that embryo r_{max}, was taken as the AVE Asymmetry Index of the embryo, with a value ranging from 0 to 1:

$$\text{AVE Asymmetry Index} = \frac{r_{cent}}{r_{max}}$$

As all Symmetric embryos have an AVE Asymmetry Index lower than 0.15, this value was taken as the threshold for evaluation of 3D-geec embryo development at D2 based on AVE asymmetry. The AVE Asymmetry Index for each D2 embryo was calculated as described, and the percentage of embryos evaluated as having successfully specified body axis was 67% ($n = 18$) (Figure 4).

Dynamics of pro-amniotic cavity formation

Apical domain detection was performed in 3D using manual Spots generation. Spots objects were generated based on Ezrin-mCherry reporter signal, and their 3D coordinates were used to calculate their distance from the embryo center, scaled by the average radius of the EPI tissue at the respective time points (Figure 6M).

Analysis of cell dynamics in the EPI

Ten EPI cells in a cluster before ExE invagination in an H2B-GFP;mT embryo were tracked over 16 hours. The mean displacements of these cells in 3D from the centroid over time were calculated as an indicator of cell dispersion (Figure S5A).

Analysis of signaling activity in the EPI

Immunostaining of Id1 was used as a readout for BMP signaling. The reporter lines Dusp4-T2A-mVenus and A_7-Venus were used as readouts for FGF-Dusp4 and Nodal-Foxh1 signaling, respectively. As signaling activity is heterogeneous within the EPI tissue, we used a proportion of cells in a high expression state as a readout of local signaling activity in the tissue. Intensity measurements were performed on a Z-projection of 10 μm slices around the equatorial plane of the embryo, processed to subtract background using a rolling ball of radius 100 px (pixel size of 0.165 μm/px). Circular ROIs were drawn on EPI nuclei in the resultant image so that each ROI was of the largest diameter that fits in the nucleus, and care was taken to avoid including regions where two nuclei overlapped due to Z-projection. The mean signal intensity in the Id1 or Dusp4-T2A-mVenus and Hoechst channels of each ROI was measured, along with the coordinates of its center. ROIs were segregated into either the proximal half or the distal half of the EPI based on their position. Due to EPI being misshapen in the absence of ExE, the left and right 20% of cells were discarded from the analysis. A cell with a Hoechst-normalized Id1 or Dusp4-T2A-mVenus signal intensity higher than the median value of all EPI cells in the embryo was annotated as $Id1^{high}$ or $Dusp4^{high}$. The percentage of $Id1^{high}$ or $Dusp4^{high}$ cells in the proximal and distal halves of each embryo was calculated and correlated with each other by a solid black line to represent the signaling landscape (Figures 7C and 7D).

Analysis of FGF-Dusp4 signalling landscapes in embryos after immunosurgery

Image acquisition and pre-processing were performed as described above for Dusp4-T2A-mVenus embryos after immunosurgery. After cropping out the EPI area, a linear ROI was set, radiating from the centre of the EPI, and rotated clockwise around the image at steps of 1°. The mean signal intensity in the Dusp4-T2A-mVenus and Hoechst channels was measured and averaged for each ROI, so that 360 pairs of intensity measurements are generated for each embryo. The intensities were normalized to the mean intensity in each channel for each embryo, and the ratio of the intensity in the Dusp4-T2A-mVenus channel to the intensity in the Hoechst channel was calculated for each ROI. The deviation of the intensity ratio from the mean intensity ratio across the embryo is calculated for each ROI and plotted against the angle of that ROI to visualise the spatial pattern of Dusp4 signalling in the EPI tissue.

Machine-learning-based segmentation and analysis

The segmentation pipeline used to process the 3D images of the mTmG membrane signal consists of four steps. In the first step the 3D input images are pre-processed, where every Z-slice is down-sampled by a factor of 4 along each axis by locally averaging squares of 4×4 pixels. The resulting images display the same physical volume with a dimension of 512×512×400 voxels and a physical voxel size

of 0.832×0.832×1.000 μm^3 (X,Y,Z). In the second step a neural network implementation from PlantSeg is used to generate a probability map of the membrane locations. In the third step the probability maps are segmented using a set of algorithms provided by PlantSeg (Wolny et al., 2020). The best segmentation algorithm and its corresponding hyper-parameters were found by a custom-made pipeline which explored thousands of different configuration parameters simultaneously using EMBL's computing cluster. In the fourth step the EPI cell segmentation output is manually selected through visual inspection, followed by manual correction as appropriate, and used for further analyses.

Since no ground truth segmentation was initially available, performance of the complete segmentation pipeline was improved by the following iterative procedure. In the first iteration a pre-trained neural network available in the PlantSeg package was used to generate the initial membrane probability maps. In particular, we used a CNN trained on the Arabidopsis ovules dataset (https://osf.io/w38uf) named "confocal_unet_bce_dice_ds2x". Having the cell boundary prediction, the initial segmentation was produced with PlantSeg. The segmentation results were improved by choosing the most correctly segmented volumes (inspected visually) and using them as ground truth labels to train a dedicated neural network for the membrane prediction task. The process of choosing the best segmentation results and re-training the network was performed four times.

Analysis of cell parameters was performed using Python 3.8 based on the segmentation generated by the above process. From two representative H2B-GFP;mT embryos live-imaged (Figure 5B), segmentations of EPI cells were picked up every 20 min until pro-amniotic cavity expansion and used for analysis with tracking lineages based on 3D coordinates of nuclear signal. Daughter cells that cannot be tracked with confidence through a mitotic event are excluded from analysis. Aspect ratio is calculated by fitting an ellipsoid to the cell and dividing the longest axis (LA) of the ellipsoid by the average of its two shorter axes (SA and MA, not depicted). Long-axis alignment is calculated as the angle between the LA of the cell and a line segment connecting the outermost voxel of the cell to the center of the cell. A low angle indicates an alignment of the long axis along the inside-outside axis of the egg cylinder.

For the analysis of neighbour effects, one lineage where the daughter cells (#1A, 1B, 1C, and 1D) remain in close proximity to each other through time and exhibit synchronous elongation and radial alignment was identified. A distinct lineage with one of daughter cells (#2C) coming to close proximity with cells #1A—1D, was picked up for analysis, and the shortest distance in 3D between each daughter cell (#2A—2F) and the centroid of the #1A—1D cell cluster was calculated using their 3D coordinates of nuclear signal. Figures 6I–6K show only cells #2A, 2C, and 2F for better visibility.

Derivation of optimal initial cell number threshold

A confusion matrix for each threshold level from 0 to 230 cells (with intervals of 10 cells) was constructed with the following definitions:

True positives (TP): D0 embryos *above* a threshold that yield egg cylinders

False positives (FP): D0 embryos *above* a threshold that do not yield egg cylinders

True negatives (TN): D0 embryos *below* a threshold that do not yield egg cylinders

False negatives (FN): D0 embryos *below* a threshold that yield egg cylinders.

The threshold level that yields the highest Accuracy (i.e., $(TP + TN)/(TP + FP + TN + FN)$) provides the best tradeoff between sample retention and egg cylinder formation efficiency. As such, a threshold of ≥ 110 cells provided the highest optimality, qualifying 66% of E4.5 embryos recovered from natural mating and resulting in 74% egg cylinder formation efficiency ($n = 35$) (Figure S2K).

Statistical analysis and data reproducibility

Experiments in this study were performed at least at three independent times, except for the data shown in Figures S2L and S5B. *N* values represent the number of independent experiments, while *n* values represent the total number of embryos collected from independent experiments, unless specified otherwise. Performance of 3D-geec was independently replicated by two operators, T.I. and HT.Z. Data analysis and statistical tests were performed in Rstudio or OriginPro. Details of the statistical analysis are provided in the figure legends. Briefly, the normality of the distribution for each dataset was tested by the Shapiro-Wilk test. When the data followed a normal distribution, difference among groups in comparison was examined by either t-test (for comparison of two groups) or one-way ANOVA (for comparison of more than two groups) followed by Tukey's post hoc test. Otherwise, nonparametric Kruskal-Wallis ANOVA was used with Mann-Whitney *U*-test. No statistical method was used to predetermine the sample size. Experiments were not randomized, and the investigators were not blinded to allocation during the experiments and outcome assessment. Data visualization was also performed in Rstudio using the ggplot2 package or OriginPro. Box and whisker plots show the following: boxes represent the 25^{th} and 75^{th} percentile range, whiskers represent the 1.5x interquartile range.

Comparison of trends in embryos developed in utero versus 3D-geec

The statistical significance of the slopes between *in utero* and 3D-geec embryos was tested by two-way analysis of variance (ANOVA) in Rstudio. Data from E4.5 embryos was excluded as no corresponding data for 3D-geec embryos exists (Figures S3B and S3C).

Analytical calculations

Analysis and plotting for Figures 7F–7H was performed with Wolfram Mathematica 12.1.1.0.